

Towards the near-infrared detection of exoplanets

Jason James Neal

Tese de doutoramento apresentada à
Faculdade de Ciências da Universidade do Porto
Astronomia
2018

TOWARDS THE NIR DETECTION OF EXOPLANETS

by

Jason James Neal

A thesis submitted in conformity with the requirements
for the degree of Doctor of Philosophy
Graduate Department of Departamento de Física e Astronomia
University of Porto

© Copyright 2018 by Jason James Neal

*To my wife Jessica,
children Timothy and Amelia;
For always supporting me.*

Acknowledgements

First I would like to acknowledge my supportive wife Jessica, and children Timothy and Amelia for bearing with me and supporting me through this journey to a distant land. For all the late nights and trips away, and a mentally exhausted presence; it is now finally over.

I would also like to acknowledge my supervisors and group leader, Pedro, Claudio and Nuno for their patience, wisdom, support and guidance throughout these last four years.

I acknowledge support from Fundação para a Ciência e a Tecnologia (FCT) through the PhD::Space fellowship PD/BD/52700/2014. Without this fellowship we could not have moved halfway around the world to come to Portugal for me to undertake this research. I was also supported by the short term contract with reference CIAAUP-20/2018-BIM.

This work was undertaken within the Exoplanet team in the Institute de Astrofísica e Ciências do Espaço and Centro de Astrofísica da Universidade do Porto. This team was supported by Fundação para a Ciência e a Tecnologia (FCT) (Portugal) research grants through Portuguese funds and from FEDER - Fundo Europeu de Desenvolvimento Regional, through COMPETE2020 - Programa Operacional Competitividade e Internacionalização (POCI) by the following grants:

UID/FIS/04434/2013

PTDC/FIS-AST/1526/2014

PTDC/FIS-AST/7073/2014

POCI-01-0145-FEDER-007672

POCI-01-0145-FEDER-016886

POCI-01-0145-FEDER-016880

POCI-01-0145-FEDER-028953

POCI-01-0145-FEDER-032113 (**G.EANES**).

ARE there any GRANTS listed here that should not be here or any missing. (team ones that I benefited from through flights etc.)

Abstract

The contents of this work focus on detecting exoplanets in the nIR.

It starts of with reduction of nIR spectra from CRIRES.

In Chapter 6 a differential subtraction technique is attempted to separate the spectra from the faint companion. Contrasting the result to other recent detections. In Chapter 7 a second technique is developed in which the BD companions are attempted to be recovered from the near-infrared spectra by fitting to a complex model of two synthetic stellar spectra. Finding the technique unsuitable for the data on hand.

Focusing on BD as they should have a stronger flux ratio than planets.

In Chapter 8 the focus is changed towards RV precision of M-dwarf stars in the nIR. Calculating the theoretical precision of stellar spectra. Useful for the next-generation of near-infrared spectrographs to detect planets around M-dwarf stars.

Some thought on future are also provided.

Resumo

Thesis abstract in Portuguese

Todo list

■	iii
■	xvii
■	references here would be nice	1
■	I am wondering if you could not here already talk a bit about different approaches, mentioning that the NIR is one of the most promising ones.	1
■	Some of the currently known exoplanet systems with the smallest radii and lightest mass have been detected through transit and later confirmed with high-precision RV follow-up (e.g. Queloz et al., 2009; Pepe et al., 2013; López-Morales et al., 2016; Ment et al., 2018).	5
■	The identification of unresolved multiple stars, such as a binary or an unrelated background star, can be achieved through high-resolution spectroscopy in which the spectral lines of individual stars can be separated (Kolbl et al., 2015). This is important to measure the correct radii of exoplanets as the extra light contribution from an unresolved secondary star will reduce the transit depth, mimicking a smaller transiting planet.	5
■	The presence of star spots on the surface of a star can be observed during transit. A star spot is a dark region on the stellar surface due to magnetic fields, which decreases the luminosity slightly. Examples of spots can be seen in the middle of the Sun from an image of the 2012 transit of Venus in Figure 1.4 (left). It shows several dark sunspots alongside Venus, although Venus did not cross them. Unlike for other stars, sunspots are spatially resolved. If an exoplanet passes in front of a spot, the luminosity decrease from the spot is temporarily hidden and a small bump occurs in the transit shape. The presence of spots in successive transits (see Figure 1.4 (right)) can indicate the alignment of the stellar rotation to the planet orbital plane (Sanchis-Ojeda et al., 2013). In this simulation an orbit aligned with the stellar rotation and the transit crosses the spot in four successive orbits. In a misaligned case a spot would only be observed in one transit.	5
■	be sure to separate "distance" from star to planet from "distance" from us to the system.	7
■	planet	9
■	some references to illustrate?	10
■	there are also works by Antonio Garcia Munoz about these phase shifts.	11
■	You never mentioned the works of Martins et al. Since this is a result from Porto, I suggest you add a small paragraph about them.	15

■ All this is correct and fine. But since you focused more in NIR, why do not have a whole section about using NIR high resolution spectroscopy as a way to detect exoplanet atmospheres? You can start such a section by something like (The development of new high resolution spectrographs operating in the infra-red opens a whole new window to the study of exoplanets.) And then you put the results of Snellen and explain the method a bit. Anyway: this is just a suggestion to start already focusing on the main subject of the thesis.	15
■ you could mention here that evaporation has been also invoked to explain some planet properties (see Fulton gap or neptune desert)	16
■ I would suggest you make a new section here! Maybe called: Brown-dwarfs: bridging the gap. And this text is perfect for that section. Maybe actually you can add a bit more stuff inside (more details about some of the things you say). This suggestion is to allow the reader to make the bridge between the planets (all you talked up to now) and the brown-dwarfs (that you tried to study in your thesis).	16
■ Pedro: I would only note that you can provide a more detailed description on the importance of determining RV information content measurement (at the very end of the chapter)	18
■ Nuno: I just think it would be good if you could make the bridge to Brown-Dwarfs and to NIR spectroscopy a bit stronger. Some of the comments and suggestions go in that direction. But since this is an overall suggestion, its not very easy to find the best way through. The general impression one has when reading the introduction is that the thesis is about planets. But then one realizes it is not. But that comes late.	18
■ I think at this point you can backtrack a bit and say that you (want to discuss how to measure RVs) from spectra.	23
■ Derived for non-resolved spectra – ????.	24
■ In high resolution RVs this tends to R^{-1} indicating the higher precision at the expense of wavelength coverage is desired	24
■ I would expand a bit on how it is important for the derivation of meaningful values for precision for future spectrographs, informing technical choices such as the wavelength range.	25
■ The first is the telescope	26
■ I find that this paragraph is a bit too dense, with many different concepts; I would propose to expand a bit more on it, and make it less dense.	27
■ Please explain that the Resolution corresponds to the FWHM of a non-resolved line (see my course) and introduce the concept of FWHM, that you use right after.	27
■ explain Nyquist, minimum information, most instruments are	28
■ The basic principles of spectroscopy are the same for optical and infrared are the same one difference is the design of the detector.	28
■ at any time	29
■ I would add a note on how near-IR spectrographs are, by definition, temperature controlled, and that has a very positive impact on the precision of RV measured with it.	30
■ There is something missing that is very different between these spectrographs: simultaneous wavelength range. In this CRIRES is clearly the worst.	31
■ infrared but also have less stable optical spectra due to convection; infrared spectra are less affected by the stellar activity.	33

■ I would expand a bit on the differences between the different spectrographs. You can start from the table.	33
■ Fix title of plot Telluric correction by different models	37
■ Figure 4.7 needs improved style	44
■ Pedro it is my understanding that the ESO pipeline did not exist/was not publicly available when you created DRACS, correct?	51
■ I am not sure if this is the best location for this section. Or it should come after the technique.	71
Figure: simulated example of combined binary spectra, and the subtraction, with a clear companion visible	73
■ check result	73
■ change RV scale for hd4747 orbit	78
■ Fix plot titles	78
■ Check M2sini labels - can we get M2 only for those that we know	78
■ Should RV of companion be scale by m2sini only or m2 if known?	78
■ Radii of different parameters	89
■ Find the wavelengths of some missing lines in the Mismatch, what elements do they belong to	99
■	100
■ Is another summary needed here? transition to next chapter	107
■ remove duplication	107
■ rv method	107
■ put in introduction??	107
■ derivation of rv?	107
Figure: An example from Figueira et al. 2016	108
■ we	108
■ we	108
■ our	108
■ our	108
■ we	108
■ add δA to plots	108
■ intensity change from connes is vertically in the slice d lambda	108
■ Finish this equation (9 of bouchy 2001)	110
■ Try the symbolic package from PC	110
■ explain snr	111
■ It is convenient to use this version when comparing observed spectra with different SNR.?	111
■ Does spectrograph pipelines such as HARPS use these equations to measure estimate/precision?	111
■ It is convenient to use this version when comparing observed spectra with different SNR.?	112
■ we	112
■ top view diagram of rotation?	112
Figure: Example of CARMENES spectra before and after correction	114
■ Add figure here	115
■ Add figure here	115
■ finish this	115
■ we	118

works of software testing in research.	118
we	119
our	119
we	120
we	122
cite the equation when I refer to it	123
Check this if it is previous	123
Should I show the working of analytical working out of this in an appendix, or here?	124
did I check this was equivalent	124
put this some where	124
put this line elsewhere.	124
add conclusions not affected	125
we	125
we	126
is this needed	126
SNR plot/diagram	126
we	126
we	126
.	126
Check how to cite priv communication properly	127
our	127
Fix up when accepted	127
we	127
comparison of plots	127
Change to 55 m s^{-1} upper limit?	127
NIR analysis work	129
reduce this for the conclusions	129
Precision table needs fixed up	131
reread and fix up still	163
Fix up at end	166
add published Ulmer-moll version	171

Contents

Todo list	vi
List of Tables	xiv
List of Figures	xv
1 Introduction	1
1.1 Towards the characterization of exoplanets	1
1.2 Exoplanet detection methods	2
1.2.1 Radial Velocimetry	2
1.2.2 Transit method	4
1.2.3 Direct Imaging	6
1.2.4 Astrometry	7
1.2.5 Microlensing	8
1.2.6 Pulsar timing	9
1.3 Detecting atmospheres	10
1.3.1 Occultation and phase variations	11
1.3.2 Transmission spectroscopy	12
1.3.3 High resolution spectroscopy	14
1.4 The diversity of exoplanets	15
1.4.1 Brown Dwarfs: bridging the gap	16
1.5 Motivation for this thesis	18
2 Radial Velocity	19
2.1 Keplerian Orbits	19
2.1.1 Mass function	21
2.1.2 Binary mass ratio	22
2.2 Measuring the RV	23
2.3 RV precision	23

3	Near-infrared spectroscopy	26
3.1	Spectrograph basics	26
3.2	The detectors	28
3.2.1	Spectrograph cooling	29
3.3	CRIRES	30
3.4	The new generation	31
3.4.1	CRIRES+	32
3.4.2	CARMENES	32
3.4.3	NIRPS	33
3.4.4	SPIRou	33
4	Atmospheres and Models	34
4.1	Earth’s atmosphere, in the nIR	34
4.2	Telluric correction	36
4.2.1	TAPAS web service	37
4.2.2	Requests for this work	38
4.2.3	Issues with TAPAS	38
4.2.4	Telluric masking	39
4.3	Synthetic Stellar models of cool stars	40
4.3.1	PHOENIX-ACES models	40
4.3.2	BT-Settl	41
4.3.3	Model access	42
4.3.4	Comparing models	43
4.4	Evolutionary models	44
4.4.1	Estimating Companion-host Flux ratio	45
4.4.2	Baraffe tables	46
5	Spectroscopic reduction	47
5.0.1	nIR reduction concepts	47
5.0.1.1	Dark Current	48
5.0.1.2	Flat-field	48
5.0.1.3	Nodding and Jitter	49
5.0.2	Th-Ar lamp calibration	49
5.0.3	Extraction	50
5.1	Pipeline Comparison	51
5.1.1	ESO CRIRES pipeline	51
5.1.2	DRACS	52
5.1.3	Pipeline comparison and selection	53
5.1.3.1	Reduction issues	53
5.1.4	Reduction experience:	57
5.2	Post reduction stages	58
5.2.1	Wavelength calibration	58
5.2.2	Telluric correction	63
5.2.2.1	Separate H ₂ O scaling.	63

5.2.3	Wavelength masking	63
5.2.4	Barycentric RV correction	64
6	Separating the spectra of faint companions	65
6.1	Spectral separation techniques	65
6.2	Motivation and target selection	66
6.2.1	The Data	69
6.2.2	CRIRES data	69
6.2.3	Calculation of expected RV	71
6.3	Direct Subtraction Method	72
6.4	Results of spectral differential analysis	74
6.4.1	Relative differential amplitude	76
6.5	Orbital Solutions	77
6.5.0.1	Differential scheduling challenges	82
6.6	Contrast to other works	82
6.7	Direct recovery in the mIR	83
6.8	Summary	84
7	Synthetic companion recovery	85
7.1	Binary χ^2 spectral recovery	85
7.1.1	The χ^2 method	85
7.1.2	Computed model spectra	86
7.1.2.1	Single component model	87
7.1.2.2	Binary model	87
7.1.2.3	Effective radius	88
7.1.3	Re-normalization	89
7.1.4	Reducing dimensionality	89
7.2	Simulation and results	90
7.2.1	Simulated binaries	90
7.2.2	HD211847 observation	93
7.2.3	Companion injection-recovery	95
7.3	Discussion	98
7.3.1	Mismatch in synthetic models	98
7.3.2	Line contribution of faint companions	99
7.3.3	χ^2 asymmetry	100
7.3.4	Component RV separation	102
7.3.5	Wavelength range	102
7.3.6	The BT-Settl models	104
7.3.7	Impact of $\log g$	104
7.3.8	Interpolation	106
7.3.9	Contrast to other works	106
7.4	Summary	107

8	Information content of nIR Spectra	107
8.1	Overview	107
8.1.1	Fundamental photon noise limitation	108
8.1.2	Prepare PHOENIX aces models	112
8.1.3	Rotational convolution	112
8.1.4	Instrumental Convolution	113
8.1.5	Numerical Convolution	113
8.2	114
8.2.1	Bands	115
8.2.2	Comparing models to CARMENES.	115
8.3	Metallicity $\log g$ effects	116
8.4	Updating RV precision software	118
8.4.1	Automated testing	118
8.4.2	Performance	118
8.4.3	Model extension	119
8.5	Numerical Gradient	119
8.5.1	Masking Function	123
8.5.1.1	Masking order	124
8.5.2	Atmospheric masking bug	124
8.5.3	SNR scaling	125
8.6	SPIRou and NIRPS ETC	126
8.7	Updated Figueira 2016 results	127
8.8	metallicity / $\log g$ extension	127
8.9	Application to CARMENES spectra	127
9	Conclusions	128
9.1	Conclusions from Paper	128
9.2	Future Work	129
9.2.1	Future implementation	129
9.2.1.1	High resolution instrumentation	129
9.3	Conclusions from paper	130
A	RV Precision Tables	132
B	Artefacts in Optimal Extraction	155
C	Multi-detector wavelength calibration	161
C.1	Comparing variable gaps	163
D	Vacuum wavelengths	165
E	PhD output	166
E.1	Publications	167
E.2	Talks and Seminars	172
E.3	Posters	173

E.4 Attended Conferences and Schools	176
E.5 Outreach	178
E.6 Other	179
Bibliography	180

List of Tables

2.1	Induced radial velocity semi-amplitudes.	22
3.1	Properties of popular optical/IR detector materials.	28
3.2	Summary of high-resolution nIR spectrographs.	32
4.1	Standard infrared pass-bands.	34
4.2	PHOENIX-ACES parameter space.	41
4.3	BT-Settl parameter space.	42
4.4	Companion/host flux ratios.	45
6.1	Stellar parameters of host stars.	68
6.2	Orbital parameters of companions.	68
6.3	List of CRIRES observations.	70
6.4	Semi-amplitude and RV separation of companions.	71
7.1	χ^2 simulation results.	91
7.2	Upper mass limits from χ^2 simulations.	97
7.3	Analysis of spectral line depths.	100
8.1	Selection of targets from the CARMENES library.	115
8.2	CARMENES targets for RV precision analysis.	115
8.3	Effect of numerical gradient.	121
8.4	RV precision with different splitting.	125
A.1	RV precisions for the PHOENIX-ACES and BT-Settl spectral libraries.	133
A.2	RV precisions calculated for the SPIRou ETC.	139
A.3	RV precisions calculated for the NIRPS ETC.	142
B.1	Identification of nod spectra artefacts.	156
B.2	Nod position tally of artefacts.	156
C.1	Example of multi-detector fitting parameters and correlation.	163

List of Figures

1.1	Number of exoplanet detections per year separated by method.	2
1.2	The RV method.	3
1.3	Exoplanet discovery year verses exoplanet mass.	3
1.4	Transit of Venus and successive transit corssings.	6
1.5	Direct detection of four exoplanets around HR 8799.	7
1.6	Modelled astrometric path on the sky.	8
1.7	Microlensing magnification of OGLE2005-BLG-390.	9
1.8	Flux contribution from a star and planet in a transiting exoplanet system.	10
1.9	Exoplanet phase variations and temperature map.	11
1.10	Transmission spectroscopy diagram.	12
1.11	Transmission spectra for several Hot-Jupiter exoplanets.	13
1.12	Cross-correlation signal from CRIRES observations of HD 209458 b.	14
1.13	Mass-Radius diagram for rocky planets with composition contours.	16
1.14	Mass-Radius relationship with probabilistic fit.	17
2.1	The basic elements of the Keplerian orbit.	20
2.2	Elements of an elliptical orbit.	21
3.1	Basic components of a spectrograph.	26
3.2	Dispersion mechanisms.	27
3.3	Schema differentiating CCD and CMOS detectors.	29
3.4	Side by side comparison of the NIRPS and SPIRou spectrographs.	30
3.5	CRIRES layout schematic.	31
3.6	CRIRES/CRIRES+ detector focal plane arrays.	32
4.1	Telluric absorption map from 0.3–30 μm at $R \sim 10\,000$	35
4.2	Telluric correction applied using the Molecfit, TelFit and TAPAS.	37
4.3	Telluric spectra for the H_2O and non- H_2O species.	38
4.4	Difference in successive PHOENIX-ACES spectra around 5000 K.	42
4.5	Large scale comparison between the PHEONIX-ACES and BT-Settl spectra.	43
4.6	Comparision of the spectrum of Arcturus to synthetic spectra.	43
4.7	Comparision of the spectrum of 10 Leo to synthetic PHOENIX-ACES spectrum.	44

5.1	Example dark frames for different exposure times.	47
5.2	Example of flat-field correction.	48
5.3	Illustration of the nodding technique.	49
5.4	Example Th-Ar calibration lamp frames for each detector.	50
5.5	Comparison between DRACS and ESOs reduction pipeline output.	54
5.6	Example of DRACS artefacts in the optimally extracted spectra HD 162020.	55
5.7	Artefacts comparison with and altered pipeline parameter.	56
5.8	Example of telluric corrected spectrum of HR 7329-B using TAPAS.	58
5.9	Example of the wavelength calibration using the synthetic telluric spectra.	61
5.10	Example reduced CRIRES spectra for each target.	62
6.1	Example of the spectral differential technique.	75
6.2	Simulated relative amplitude of differential spectrum.	77
6.3–6.11	RV curves for the host and companion of each target.	79
7.1	χ^2 contour for companion recovery of a simulated Sun - M-dwarf binary.	91
7.2	χ^2 contour for companion recovery of a simulated observation of HD 211847.	92
7.3	χ^2 contour for an observation HD 211847.	95
7.4	Comparison between observation of HD 211847 and the best fit synthetic binary model.	96
7.5	Result of simulated injection-recovery of synthetic companions on HD 30501.	98
7.6	Shape of simulated χ^2 with different injected companion temperatures.	101
7.7	PHOENIX-ACES spectra for temperatures between 2500 and 5000 K, corresponding to the same lines in Figure 7.6. The flux units are the native units of the PHOENIX-ACES spectrum, ($\text{erg s}^{-1} \text{cm}^2 \text{cm}^{-1}$), and have not been scaled by the stellar radii. All spectra have a $\log g=5.0$ and $[\text{Fe}/\text{H}]=0.0$. The vertical dotted lines indicate the edges of the CRIRES detectors.	103
7.8	Detector #1 spectrum for HD 211847 (blue) alongside the PHOENIX-ACES (orange dash-dot) and BT-Settl (green dashed) synthetic spectra for the host star only, with parameters $T_{\text{eff}}=5700 \text{ K}$, $\log g=4.5$ and $[\text{Fe}/\text{H}]=0.0$. Both synthetic models have been normalized and convolved to $R = 50\,000$. There is a 0.05 off-set between each spectrum	105
8.1	Demonstration of a shifted arbitrary spectral line.	109
8.2	Quality factor verse $[\text{Fe}/\text{H}]$ and $\log g$ for different spectral types and wavelength bands.	117
8.3	Comparing of numerical gradient algorithms.	121
8.4	Comparison of RV precision results to Figueira et al. (2016).	127
B.1–B.7	Extra examples of reduced spectra with artefacts. One for each target.	157
C.1	Multi-detector fit and difference to individual fits.	162
C.2	Difference of multi-detector combined fit to the individual calibration mappings.	162
C.3	Multi-detector calibration parameter correlations.	164

Separating the spectra of faint companions

Spectral observations of binary systems contain the spectra of both bodies, in proportion to their flux ratio, and Doppler shifted relative to each other due to their orbital motion. There are many different techniques to disentangle the spectra of binary objects. This chapter focuses on applying a direct subtraction method to near-infrared (nIR) spectra of FGK stars which have Brown Dwarf (BD) companions, with the goal to isolate the spectrum of the companions. The data used was obtained with the CRIRES instrument in 2012¹ observed with the purpose to apply the differential technique specifically. A level of trust was placed in the quality of the observations, which was unfortunately misplaced. This chapter begins with the motivation for these specific targets and details the observations obtained. The direct subtraction technique will be presented and its application to the observations will be explored. The limits of the differential technique at low RV separations is given by simulation with synthetic spectra.

6.1 Spectral separation techniques

Spectral observations of binary systems contain the spectra of both bodies, in proportion to their flux ratio, and Doppler shifted relative to each other due to their orbital motion. There are many other disentangling techniques to separate mixed spectra of binary systems, (e.g. Hadrava, 2009, and references therein). These techniques were initially developed to identify and separate the spectra of binary stars, however the techniques and instrumentation have improved so that lower flux ratios from smaller BD and giant planet companions have begun to be detected. A small variety of these techniques will be briefly presented below before exploring the techniques used in this work in more depth.

Several disentangling techniques work on deriving the spectral components from several spectra at different orbital phases. At the minimum $n + 1$ observations can be used to set up a system of linear equations to solve for n spectral components. This can be solved using singular value decomposition SVD (e.g. Simon et al., 1994; Sablowski et al., 2016). These work best with many well spaced observations, for example Sablowski et al. (2016) state their ideal situation is homogeneous samples over at least half the period, to identify the moving spectral components.

Tomographic techniques (e.g. Bagnuolo et al., 1991) and Fourier techniques (Hadrava, 1995) have also been developed for disentangling a series of binary spectra. Recently this has even been performed

¹ Before this thesis began

using Gaussian processes which simultaneously fits stellar (or exoplanet) orbits as well as their spectral components (Czekala et al. (2017)).

A fairly common technique for deriving precise radial velocities of spectral components in binaries is to apply cross-correlation against a library of known spectra. TODCOR (TwO-Dimensional CORrelation) (Zucker et al., 1994) is a commonly used algorithm for cross-correlation of two spectral components and revealing the faint secondary. It has been simulated to be able to detect secondaries with flux ratios down to $\sim 1/1000$ provided a sufficient SNR (e.g. Mazeh et al., 1994; Mazeh et al., 1997). TODCOR requires knowledge of the two spectral components, a series of spectral templates are used to correlate against the observation. These can either be other observed stellar spectra or synthetic spectra, with the highest correlating spectral pair indicating the two components.

Recently this has been used to detect the emission spectra of non-transiting giant planets. Lockwood et al. (2014) and Piskorz et al. (2016) apply TODCOR, with exoplanet spectrum templates for the companion, to a several epochs of high resolution and high SNR nIR spectra. Combining together the individual results in a maximum likelihood framework to obtain the orbital solution of the components.

χ^2 fitting observations to a library of spectra can also been performed. Kolbl et al. (2015) perform spectral fitting against the SpecMatch library of observed optical spectra, achieving an 80% injection-recovery rate for a 3500 K M-dwarf companion to an 5000–6000 K host star at a 1% flux ratio. Unfortunately a thorough high-resolution spectral library in the nIR is not currently available, requiring synthetic spectral libraries to be used in this work instead.

Other methods for spectral separation focus on removing the spectral component of the host star. Rodler et al. (2012) do this by constructing a stellar mask for the host by constructively combining the host spectra from a number of different phases. The contribution of the faint companion to the mask, added at different phases, is significantly reduced. The stellar mask is then subtracted from each individual observation to remove the hosts spectrum from all measurements, leaving the companion. González et al. (2006) present an iterative subtraction method in which the knowledge about spectral components of the host and companion are iteratively improved with successive observations and iterations.

Ferluga et al. (1997) provide an analytical approach via secondary reconstruction through a differential spectrum. Spectra from different phases are shifted to the rest frame of the host star and subtracted to mutually cancel out the spectrum of the host star allowing the two copies of the faint companion spectra to become visible. Kostogryz et al. (2013) further simulate this direct subtraction approach. Simulating CRRES observations of an M-dwarf with a low mass (likely BD) companion to recover the mass of the companion by measuring the RV separation between the companion spectra. A similar differential subtraction approach is used in this work, as the limited observations analysed are not suitable to apply the more advanced techniques that require several spectra from multiple phases.

6.2 Motivation and target selection

The work of Sahlmann et al. (2011) used the astrometry technique to identify several candidate brown dwarf companions of FGK stars with $M_2 \sin i$ values $> 10 M_{\text{Jup}}$. Seven candidates from Sahlmann et al. (2011), which were visible in Period 89 (2012), were selected for further observation in order to identify their stellar nature. That is, to refine the mass of the companions to distinguish if their companion is: a large giant planet ($M \lesssim 13 M_{\text{Jup}}$), a Brown dwarf ($13 \lesssim M \lesssim 80 M_{\text{Jup}}$), or a low-mass star ($M \gtrsim 80 M_{\text{Jup}}$).

The list target host stars that were observed are presented in Table 6.1 along with their stellar parameters, while Table 6.2 details the orbital parameters of each system from the literature.

It is noted that the orbital parameters of some targets have been refined in the literature since the observations took place. For example three candidates have had their masses refined in recent works. The companion to HD 211847 was determined to be a low mass star with $M_2 = 155 M_{\text{Jup}}$ (Moutou et al., 2017), while the companion to HD 4747 was found to have a mass of $M_2 = 60 M_{\text{Jup}}$ (Crepp et al., 2016). The two companions of HD 202206 (B and c) were found to have masses of $M_B = 93.6 M_{\text{Jup}}$ and $M_c = 17.9 M_{\text{Jup}}$, respectively, classifying HD 202206c as a “circumbinary brown dwarf” (Benedict et al., 2017). These three companions with recently refined masses, along with HD 30501, create a good set of benchmarks to compare any results from the techniques used here, and show that the masses of these targets do span the BD to low-mass star range. All target companions except HD 162020 (P=8.4 days) are in (very) long period orbits (P=0.7–38 years) with masses (or $M_2 \sin i$) greater than $10 M_{\text{Jup}}$.

Table 6.1: Stellar parameters of the host stars. V is the apparent visual magnitude taken from SIMBAD (Wenger et al., 2000). Distances were calculated using the GAIA DR2 parallax measurements.

Star	SpT	V	T_{eff} (K)	$\log g$ (cm s $^{-2}$)	[Fe/H]	M_1 (M $_{\odot}$)	Age (Gyr)	d (pc)	Reference
HD 4747	K0V	7.15	5316 ± 50	4.48 ± 0.10	-0.21 ± 0.05	0.81 ± 0.02	3.3 ± 2.3	18.80 ± 0.04	1, 2, 3, 8
HD 162020	K3V	9.12	4723 ± 71	4.31 ± 0.18	-0.10 ± 0.03	0.74 ± 0.07	3.1 ± 2.7	30.85 ± 0.06	4, 5, 6, 8
HD 167665	F9V	6.40	6224 ± 50	4.44 ± 0.10	0.05 ± 0.06	1.14 ± 0.03	$0.7 - 3.6$	31.24 ± 0.06	1, 8
HD 168443	G6V	6.92	5617 ± 35	4.22 ± 0.05	0.06 ± 0.05	1.01 ± 0.07	10.0 ± 0.3	39.67 ± 0.12	5, 6, 8
HD 202206	G6V	8.07	5757 ± 25	4.47 ± 0.03	0.29 ± 0.02	1.04 ± 0.07	2.9 ± 1.0	46.03 ± 0.14	5, 7, 8
HD 211847	G5V	8.62	5715 ± 24	4.49 ± 0.05	-0.08 ± 0.02	0.92 ± 0.07	$0.1 - 6.0$	48.81 ± 0.13	1, 2, 4, 8
HD 30501	K2V	7.59	5223 ± 50	4.56 ± 0.10	0.06 ± 0.06	0.81 ± 0.02	$0.8 - 7.0$	20.37 ± 0.01	1, 4, 8

References: (1) Sahlmann et al. (2011); (2) Santos et al. (2005); (3) Crepp et al. (2016); (4) Tsantaki et al. (2013); (5) Bonfanti et al., 2016; (6) Santos et al. (2004); (7) Sousa et al. (2008); (8) Collaboration et al. (2018);

Table 6.2: Orbital parameters for the BD companions obtained from the literature.

Object	γ (km s $^{-1}$)	Period (day)	e	K_1 (m s $^{-1}$)	T_0 (JD-2,450,000)	ω (deg)	$M_2 \sin i$ (M $_{\text{Jup}}$)	M_2 (M $_{\text{Jup}}$)	Ref.
HD 4747	0.215 ± 11	$13\,826.2 \pm 314.1$	0.740 ± 0.002	755.3 ± 12	463.1 ± 7.3	269.1 ± 0.6	39.6	60.2	1
HD 162020	-27.328 ± 0.002	$8.42819 \pm 6e^{-5}$	0.277 ± 0.002	$1\,813 \pm 4$	$1\,990.68 \pm 0.01$	28.4 ± 0.2	14.4	-	2
HD 167665	8.003 ± 0.008	$4\,451.8 \pm 27.6$	0.340 ± 0.005	609.5 ± 3.3	$6\,987.6 \pm 29$	-134.3 ± 0.9	50.3	-	3
HD 168443b	-0.047 ± 0.552	$58.1124 \pm 4e^{-4}$	0.529 ± 0.001	475.13 ± 0.9	$5\,626.20 \pm 0.02$	172.9 ± 0.1	7.7	-	4
HD 168443c	-0.047 ± 0.552	$1\,749.83 \pm 0.57$	0.211 ± 0.002	297.7 ± 0.6	$5\,521.3 \pm 2.2$	64.9 ± 0.5	17.1	-	4
HD 202206B	14.721	256.33 ± 0.02	0.432 ± 0.001	567 ± 1	$2\,176.14 \pm 0.12$	161.9 ± 0.2	17.4	93.2 ± 7.3	5, 6
HD 202206c	14.721	$1\,260 \pm 11$	0.22 ± 0.03	41 ± 1	$3\,103 \pm 452$	280 ± 4	2.3	17.9 ± 2.9	5, 6
HD 211847	6.689^a	$7\,929.4 \pm 2\,500$	0.685 ± 0.068	291.4 ± 12.2	$12\,030.1 \pm 2\,500$	159.2 ± 2.0	19.2	155	3, 7
HD 30501	23.710 ± 0.028	$2\,073.6 \pm 3.0$	0.741 ± 0.004	$1\,703.1 \pm 26.0$	$3\,851.5 \pm 3.0$	70.4 ± 0.7	62.3	89.6	3

References. (1) Crepp et al. (2016); (2) Udry et al. (2002); (3) Sahlmann et al. (2011); (4) Pilyavsky et al. (2011); (5) Correia et al. (2005); (6) Benedict et al. (2017); (7) Moutou et al. (2017)

Notes. $^{(a)}$ fixed

The spectral differential approach was chosen with the goal to constrain the companion masses while minimizing the observational time required to observe, only requiring two observations in theory. It was determined that it should be possible to obtain a detection of a companion with a 1% contrast ratio with an exposure time of around 20 minutes. Two observations at “clearly separate RVs” were requested to constrain each target. Observations were performed without telluric standard star observations to avoid the extra observing time overhead, choosing to instead rely on synthetic model correction (see Section 4.2). The *K*-band was chosen to achieve a high contrast relative to the host star, detected in the extreme V-K colour indexes (>7.8), while the specific atmospheric window (2110–2070 nm) was chosen in order to reduce the absorption introduced by the atmosphere (Barnes et al., 2008).

6.2.1 The Data

6.2.2 CRIRES data

Observations were performed with the CRIRES instrument (Kaeufl et al., 2004) configured to observe a narrow wavelength domain of the *K*-band between 2120–2165 nm. The slit width of $0.4''$ resulted in an instrumental resolving power of $R = 50\,000^2$. No adaptive optics were used to ensure that the entrance slit was entirely covered by each target. This is to prevent strong slit illumination variations that could change the shape of spectral lines.

The observations were performed in service mode during Period 89 with run ID. 089.C-0977(A) between April and August 2012. A single observation is composed of eight individual spectra with an integration time of 180s each, observed in the ABBAABBA nod cycle pattern to obtain a high signal-to-noise (>100) when combined. The list of observations obtained with CRIRES are provided in Table 6.3.

There is a slight inconsistency with **the** some of the observations, taken in service mode. For instance HD 202206 has two observations taken with the Ks filter, while one is taken with the J filter. There is also the last observation of HD 30501 taken with a different filter compared to the others. The documents for the phase two observing proposal were unable to be obtained to determine if these ‘odd’ filters were requested or if this was an observational mistake.

There is also an inconsistency with the naming or ordering of the observations again with the target HD 202206. The observation that was performed first in time is labelled with the observation name of HD 202206-3 in the fits header file, while the second and third observations are labelled -1 and -2 respectively.

There could be two possible reasons for the single observation of HD 4747. The first reason could be that only one observation was requested due to the very long orbital period of the target, although this would not have fulfilled the science goal. The second and more likely reason is that these observations were performed in service mode, as a filler program, and there was no time to observe a second observation of HD 4747.

² The rule of thumb resolution for CRIRES is $100\,000 \times \frac{0.2''}{\text{slit width}}$ with the slit width in arcseconds

Table 6.3: Details regarding each of the CRIRES observations. The number of artefacts removed in Section 5.1.3.1 as well as the SNR of the combined spectra is provided. The last three columns are the RV calculated from the orbital solution for both the host and largest companion, and the RV difference between them.

Object	Obs. #	Start date (yyyy-mm-dd hh:mm:ss)	Filter	Airmass (at start)	Artefacts / 32	SNR	RV_1 km s ⁻¹	RV_2 km s ⁻¹	rv_2 km s ⁻¹
HD 4747	1	2012-07-06 07:36:06	Ks	1.25	7	340	-0.219	-0.154	0.065
HD 162020	1	2012-07-04 06:23:22	Ks	1.30	2	127	-28.760	50.785 ^a	79.545 ^a
HD 162020	2	2012-07-04 06:57:48	Ks	1.44	2	128	-28.717	48.440 ^a	77.157 ^a
HD 167665	1	2012-07-28 05:00:53	Hx5e-2	1.24	7	371	7.581	18.024 ^a	10.443 ^a
HD 167665	2	2012-07-28 05:37:27	Hx5e-2	1.39	4	374	7.581	18.025 ^a	10.444 ^a
HD 167665	3	2012-08-05 02:54:03	Hx5e-2	1.04	4	358	7.575	18.163 ^a	10.588 ^a
HD 168443	1	2012-08-05 04:29:32	Ks	1.31	2	192	-0.121	50.932 ^{a,b}	51.053 ^{a,b}
HD 168443	2	2012-08-05 04:58:50	Ks	1.47	4	190	-0.121	51.189 ^{a,b}	51.310 ^{a,b}
HD 202206	1	2012-07-12 06:54:44	Ks	1.01	3	189	14.843	12.992 ^b	-1.851
HD 202206	2	2012-07-13 05:41:40	J	1.01	3	209	14.837	13.065 ^b	-1.772
HD 202206	3	2012-07-11 08:29:55	Ks	1.15	4	180	14.849	12.920 ^b	-1.929
HD 211847	1	2012-07-06 07:02:57	Ks	1.07	4	272	6.613	7.171	0.558
HD 211847	2	2012-07-13 06:54:37	Ks	1.05	5	283	6.614	7.167	0.553
HD 30501	1	2012-04-07 00:08:29	Hx5e-2	1.60	3	217	22.372	36.377	14.005
HD 30501	2	2012-08-01 09:17:30	Hx5e-2	1.42	10	212	22.505	35.120	12.615
HD 30501	3	2012-08-02 08:47:30	Hx5e-2	1.53	8	237	22.507	35.102	12.595
HD 30501	4	2012-08-06 09:42:07	Ks	1.28	7	235	22.514	35.031	12.517

^a Maximum RV given $M_2 \sin i$ only.

^b Largest mass companion only.

Table 6.4: Estimated orbital semi-amplitude and RV separation of the companions, given the companion mass (M_2 or $M_2 \sin i$) from Table 6.2 and observation times from Table 6.3.

Companion	Estimated K_2 (km s^{-1})	Estimated $ \Delta RV $ (m s^{-1})	Phase coverage (%)
HD 4747	-10.65	—	—
HD 162020	-98.92 ^a	2388	0.28
HD 167665	-14.47 ^a	145	0.18
HD 168443b	-64.65 ^a	258	0.035
HD 168443c	-18.05 ^a	<1	0.001
HD 202206B	-6.79	78	0.74
HD 202206c	-2.50	<1	0.15
HD 211847B	-1.85	5	0.09
HD 30501	-16.12	1410	5.8

^a Maximum K_2 only given $M_2 \sin i$.

All observations were reduced using the DRACS pipeline with the artefact corrections method applied (see Section 5.1.3). Each observation was then: wavelength calibrated using a synthetic telluric spectrum, corrected for telluric absorption, and then corrected for the barycentric RV following Sections 5.2.1, 5.2.2 and 5.2.4.

6.2.3 Calculation of expected RV

Before the differential subtraction method is presented, calculations are performed to estimate the RV of both components in each observations and the likely separation between the companions between observations. The time of each observation is used as input into Equation 2.6 **along** combined with the orbital parameters from Table 6.2 to calculate the expected RV of the host star. These values calculated are provided in Table 6.3 as RV_1 . For the companion, the mass (M_2 or $M_2 \sin i$) is used alongside the stellar mass from Table 6.1 to calculate the RV of the companion (see Section 2.1.2). This is given as RV_2 in Table 6.3. The RV difference in between the host and companion for each observation is also computed and provided as $rv_2 = RV_2 - RV_1$ although this will not be used until Chapter 7.

For these observations the maximum estimated RV separation between the two companion spectra in ΔRV is calculated following Equation 6.5 below and provided in Table 6.4. This table also contains the estimated semi-major RV amplitude for the companion K_2 (from Equation 2.14) and the phase coverage of the observations. The phase coverage is the maximum fraction of the orbit covered between the observations for each target. For HD 4747 the ΔRV and phase coverage values are missing due to the single observation.

The full orbital solution for the components along with the times of observations are displayed later in Section 6.5.

I am not sure if this is the best location for this section. Or it should come after the technique.

6.3 Direct Subtraction Method

Here the direct subtraction method used is presented. The basic premise is to take two high resolution spectra of a binary system at separate phases, transform them to the rest frame of the star and take the difference to remove the spectrum of the host star, leaving behind a residual comprised of difference of two companion spectra with different Doppler shifts. Similar techniques originally developed to separating binary stars (Ferluga et al., 1997) and has been used for a M-dwarf with a low-mass companion (e.g. Kostogryz et al., 2013).

Assuming that the instrumental profile and atmospheric absorption are dealt with appropriately the spectra of the observed targets are assumed to be composed of two spectral components: a bright host star blended with the spectrum of a faint companion. The spectrum received from the host-companion pair is given by the superposition of two spectral components (J_1, J_2):

$$I(\lambda) = J_1(\lambda - v_1) + J_2(\lambda - v_2), \quad (6.1)$$

where the subscripts 1 and 2 indicate the spectrum of the host and companion respectively, λ represents the wavelength of the spectra and $\lambda - v$ represents the Doppler shift $\lambda(1 - v/c)$ by a velocity v .

This can be shifted into the rest frame of the host star by applying the shift v_1 :

$$I(\lambda + v_1) = J_1(\lambda) + J_2(\lambda - v_2 + v_1). \quad (6.2)$$

To analyse J_2 , the spectral component of interest, the component from the host needs to be carefully removed. If two observations of the same target are observed, denoted with subscripts a and b , there will be relative motion between the components due to the orbit. Assuming that the stellar spectra do not change over time³ ($J_{1a} = J_{2a}$) and each spectrum can be individually Doppler shifted to the rest frame of the host star $J_1(\lambda)$, then the spectrum of the host star can be removed through subtraction of the two observations. Mutually cancelling the host component leaves two components of the companion subtracted from each other, with a relative Doppler shift between them.

$$\begin{aligned} S(\lambda) &= I_a(\lambda + v_{1a}) - I_b(\lambda + v_{1b}) \\ &= (J_{1a} + J_{2a}(\lambda - v_{2a} + v_{1a})) - (J_{2b} + J_{2b}(\lambda - v_{2b} + v_{1b})) \\ &= J_{2a}(\lambda - v_{2a} + v_{1a}) - J_{2b}(\lambda - v_{2b} + v_{1b}) \end{aligned}$$

$$S(\lambda + v_{2a} - v_{1a}) = J_{2a}(\lambda) - J_{2b}(\lambda - v_{2b} - v_{1a} + v_{1b} + v_{2a}) \quad (6.3)$$

$$S(\lambda') = J_{2a}(\lambda) - J_{2b}(\lambda - \Delta RV_2) \quad (6.4)$$

where,

$$\Delta RV_2 = v_{1a} - v_{1b} - v_{2a} + v_{2b} \quad (6.5)$$

is the RV difference between the two companion spectral components when the host components are mutually subtracted, and $\lambda' = \lambda + v_{2a} - v_{1a}$.

The resulting differential spectra $S(\lambda')$, dubbed *s-profile* by Ferluga et al. (1997), is composed of just the companion spectra, shifted and subtracted from itself.

³ (Kostogryz et al., 2013) find the stellar activity residual is smaller than the companion differential flux.

Ferluga et al. (1997) provide an analytical form for the *s-profile* given a single Gaussian line of the form $J(\lambda) = 1 - D \cdot \exp^{-\pi(\lambda-\lambda_0)^2/W^2}$:

$$S(\lambda) = 2D \cdot \exp^{-\pi D^2[(\lambda-\lambda_0)^2+(k/2)^2]/W^2} \cdot \sinh \frac{\pi D^2(\lambda-\lambda_0)k}{W^2}, \quad (6.6)$$

where λ_0 , D , and W are the central wavelength, depth and equivalent width of the Gaussian line, and $k = \Delta RV_2$ is the shift between the two companion spectra.

From binary dynamics (e.g. Murray et al., 2010) the RV amplitudes of the host and companion (ignoring the system velocity *gamma*) are related through the mass ratio, q , while having an opposite sign⁴ (see Section 2.1.2):

$$v_2 = -q * v_1 \quad (6.7)$$

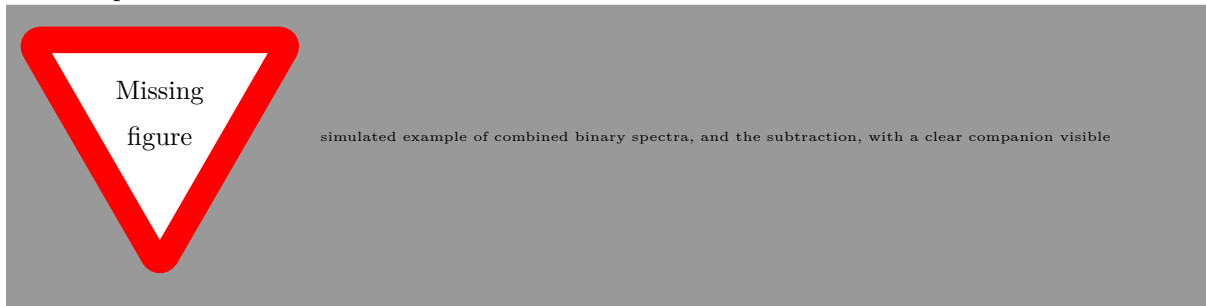
Equation 6.5 can be simplified by expressing it in terms of the mass ratio and host RV only:

$$\begin{aligned} \Delta RV_2 &= qv_{1a} - qv_{1b} + v_{1a} - v_{1b} \\ &= (1 + q)(v_{1a} - v_{1b}). \end{aligned} \quad (6.8)$$

If the ΔRV_2 between the companion spectra is able to be constrained or derived from the s-profile (see Ferluga et al., 1997) then the mass ratio of the system, q , can be determined, thereby constraining the mass of the companion.

The values v_{1a} and v_{1b} are radial velocity of the host components. The host's RV are calculated using the Equation 2.6 with the orbital parameters from the literature and provided in Table 6.2. These are used to shift each spectrum into the rest frame of the host star to mutually cancel the host's spectrum. These components can also be determined directly from the spectrum by cross-correlating the observed spectrum with a stellar template of the host and gave results in reasonable agreement. There should be checks for consistency between v_{1a} , v_{1b} and how well the host component is removed in the s-profile.

Example simulations?



This method is very similar to Kostogryz et al. (2013), which obtain two observations from the extrema of the RV curve of a M-dwarf with a low-mass companion. They also perform a number of simulations regarding observing CRIRES spectra with different brown dwarfs. Figure out the flux ratio limit they get to???

check result

It is necessary to have a consistent instrumental setup (Ferluga et al., 1997), to avoid introducing extra instrumental effects (e.g. slit-width and/or filters) into the spectral differentials and to always observe the same wavelength range and maximize the information to be extracted. For these observations,

⁴ The opposite sign arises from a 180° difference in the angle of periaapsis, ω , for the companion.

the second observation of HD 202206 and fourth of HD 30501 were taken with different filters compared to the other observations. Therefore, these two observations could not be used for this differential analysis. As noted in Hadrava (2009), any spectral differences in the filters would add extra unknown signal/noise making it harder to disentangle the faint spectral differences.

6.4 Results of spectral differential analysis

The spectral differential procedure outlined above was applied to the wavelength-calibrated, telluric- and barycenter- corrected CRIRES observations. The spectra were first Doppler shifted to the rest frame velocity of the system by applying a shift of $-\gamma$. Each spectra is then shifted by its $-RV_1$ so that the host lines are at rest. Finally one spectrum is subtracted from the other as described above.

Although this is attempted on all targets only the most favourable case, HD 30501, is shown in Figure 6.1. It is favourable because it is the second largest companion in the sample at 90 M_{Jup} but also has the second largest RV separation between observations. The top panel shows the reduced CRIRES spectrum of HD 30501 from detector 1 without telluric correction. The telluric model is also shown in the top panel. The middle panel shows the CRIRES spectra corrected with the telluric model. The differential spectra recovered for HD 30501 is shown at the bottom panel of Figure 6.1. The shaded regions indicate where the telluric green and host star blue spectra are $> 4\%$ deep. This indicates that the features of the differential spectrum near these shaded regions are likely due to imperfect telluric correction and host cancellation.

The mutual cancellation of the stellar host seems to work well for the $\sim 40\%$ deep line near 2117 nm, with the line being completely removed, but it does not do so well for the smaller $\sim 10\%$ deep line around 2121.5 nm. The residual for the large $\sim 40\%$ deep telluric line near 2118.5 nm is still quite prominent. Around 2120 nm there is wide negative residual around three neighbouring telluric lines, $\sim 10\%$ deep. One possible explanation for this is that the continuum normalization near 2120 nm was influenced by this grouping of lines.

To understand the observed differential signal simulations were performed of a differential spectrum of HD 30501 using a synthetic PHOENIX-ACES spectra with parameters $T_{\text{eff}}=2500$ K, $\log g=5.0$, and $[\text{Fe}/\text{H}]=0.0$, with the RV offset estimated from the observation times. These parameters represent an estimated companion T_{eff} with the metallicity and $\log g$ similar to the host (closest grid model). The model spectra were convolved to $R = 50\,000$, continuum normalized and scaled by the estimated flux ratio of the companion. In this simulation a synthetic host or telluric spectra is not included and as such simulates the differential result of a “perfect” host cancellation with no telluric contamination present. This is the ideal-case scenario, and it is stressed that it is impossible to simulate the effect of improper telluric correction in a meaningful way. When comparing the simulated and observed differential in the bottom panel of Figure 6.1, there is a striking amplitude difference. The orange-dashed line of the simulated differential spectrum amplitude is of a much smaller scale than the observed differential. This simulation demonstrates that the amplitude of the differential signal of HD 30501 expected is much smaller than the residuals created by the differential technique applied to these observations.

The amplitude of the differential signal is lower than expected due to the very low ΔRV between the observation pairs. The maximum ΔRV between observational pairs, for the targets investigated in this work, are provided in Table 6.4. In the best target in this sample, HD 30501, the ΔRV_2 of the companion between observations is 1.41 km s^{-1} . For comparison, a single Gaussian absorption line, to be

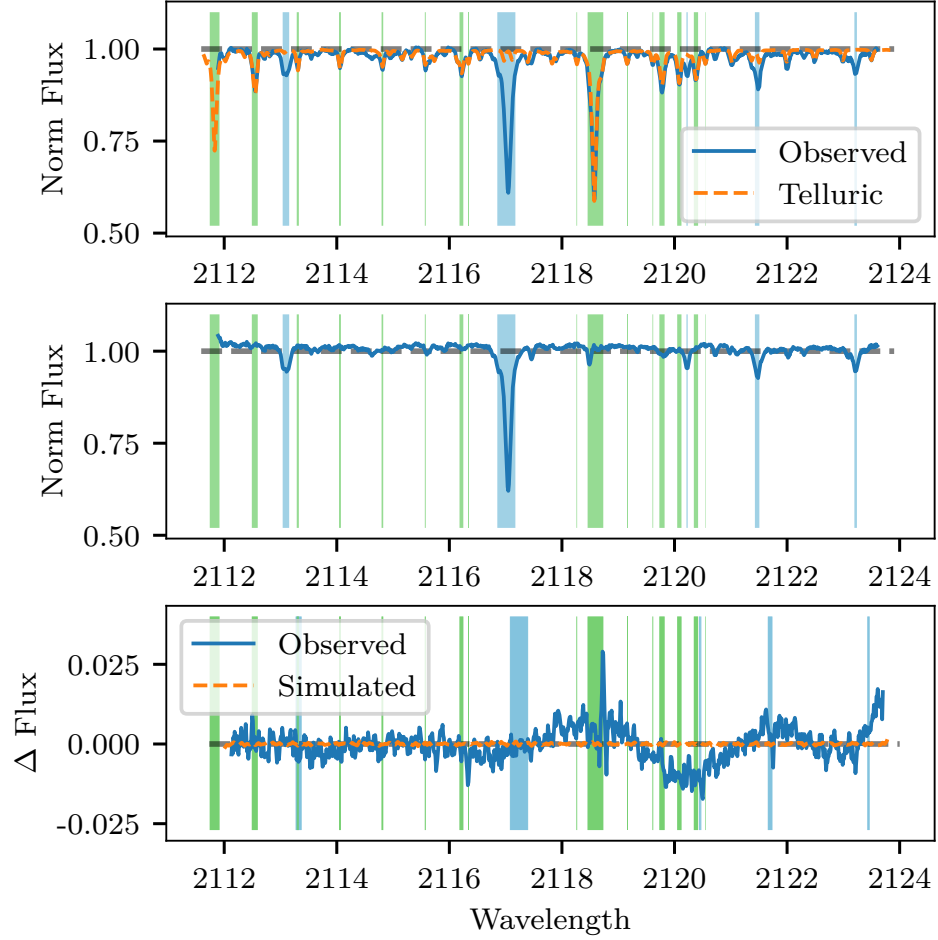


Figure 6.1: Top: A reduced CRIRES observation of HD 30501 (blue) for detector 1 between 2112–2124 nm along with the TAPAS telluric absorption model (orange dashed) used for the wavelength calibration and telluric correction. Middle: The telluric corrected spectra. Bottom: (blue) Differential spectra for HD 30501 between observations 1 and 3. (orange dashed) Simulated “perfect” differential using PHOENIX-ACES spectra with parameters $T_{\text{eff}}=2500$ K, $\log g=5.0$, and $[\text{Fe}/\text{H}]=0.0$, with the same ΔRV as the observations. The shaded regions indicate where the telluric green and host star blue spectra are $> 4\%$ deep.

shifted by $\Delta\lambda = \text{FWHM}$ would need a ΔRV of $v_{\text{FWHM}} = c/R \approx 6 \text{ km s}^{-1}$. Since the ΔRV_2 are shifted by a significant smaller value than the line FWHM, the spectral lines of the companion also mutually cancel themselves, diminishing the amplitude of the differential signal significantly. As the companion spectra are already faint (with a flux ratio at the percent level) the differential signal is not detectable in these observations at the achieved noise level.

When the ΔRV of the companion is smaller than the FWHM of a line there is a mutual subtraction of the companion spectra, diminishing the detected amplitude of the differential signal, and removing the ability to detect the companions using this method. The observations need to be spaced further apart in time/phase to achieve a larger ΔRV_2 separation and increase the amplitude of the differential. Once there is a separation there will be complex interactions between neighbouring lines that need to be accounted for.

6.4.1 Relative differential amplitude

Further investigation was performed into the differential subtraction under small ΔRV . This is done by exploring the amplitude of the differential against a variation in RV. Simulations were performed creating a differential spectra for a range of ΔRV s between $\pm 10 \text{ km s}^{-1}$ using the same PHOENIX-ACES spectra for the companion of HD 30501 ($T_{\text{eff}}=2500 \text{ K}$, $\log g=5.0$, $[\text{Fe}/\text{H}]=0.0$) convolved to $R = 50\,000$. These simulations were focus on the wavelength range 2110–2123 nm, corresponding to detector #1 of the CRILES observations. The differential spectra was created for each by taking the synthetic spectrum for the companion, Doppler shifting a copy of the spectrum and subtracting it from the original. At each RV step the maximum absolute differential amplitude (peak to peak) of the simulated differential spectrum observed was recorded. Again these simulations are performed assuming perfect telluric correction and removal of the host star by only considering the spectrum of the companion alone.

The result of this simulation is shown in Figure 6.2. As this absolute amplitude is specific to the lines present in the analysed wavelength range, the values were normalized by the median amplitude value outside of the line FWHM (dashed vertical lines), between $\pm(7 - 10) \text{ km s}^{-1}$, to give a relative differential amplitude, independent from the depth of a specific line. Differential subtraction simulations were also performed using a spectrum made up of a single Gaussian or Lorentzian line; these are shown in Figure 6.2 as the orange dashed and green dash-dotted lines respectively. The spectral profile shape of the differential for the Gaussian line was also checked for consistency with the analytical form of the differential spectra from Ferluga et al. (1997, Equation A.1) (included above as Equation 6.6).

Figure 6.2 shows that with a ΔRV of zero between companion spectra the spectral lines of the companion completely cancel each other out, resulting in zero amplitude. As the RV separation increases in either direction, the individual lines stop completely cancelling begin as they begin to separate. A maximum differential amplitude is achieved when the individual lines are fully separated. The shape/width of the differential spectral lobes Ferluga et al. (e.g. 1997, eqn. A.1) was not considered, but this could also have been measured.

At simulated separations beyond 10 km s^{-1} the neighbouring spectral lines begin to strongly interfere, leading to a variable (quasi-sinusoidal) relative amplitude, although this is not shown here. The shape of the relative amplitude becomes complicated due to the line interaction and because the ΔRV for all observations fall well short of this region it was not investigated further. It is suspected that the interaction of neighbouring lines is one possible cause for the difference in the relative differential amplitude between the single theoretical line profiles and synthetic spectrum between 2 and 6 km s^{-1} .

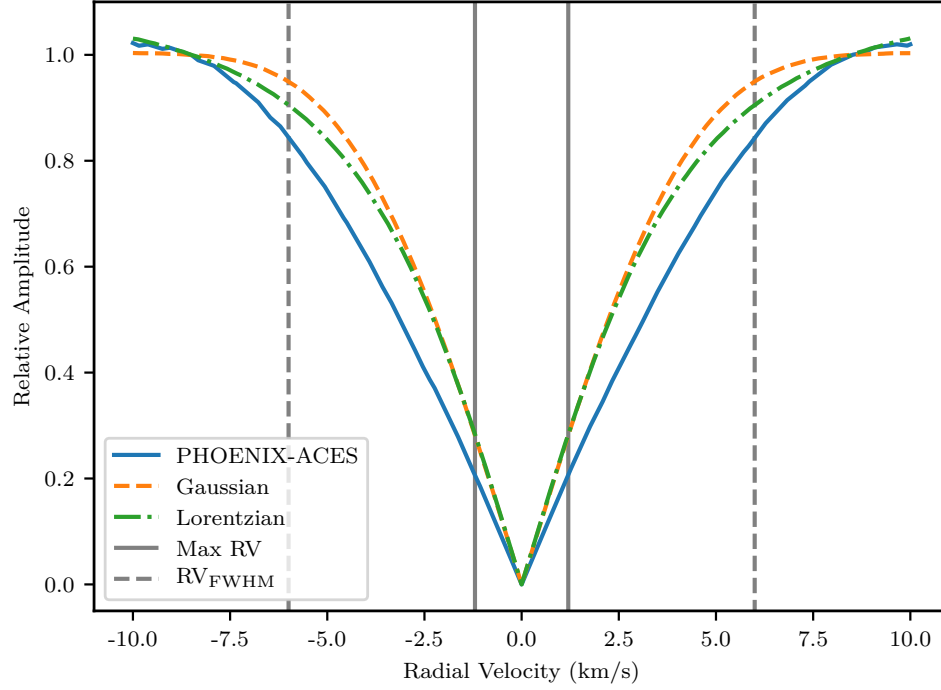


Figure 6.2: Simulated relative amplitude of differential spectra at different companion ΔRV separations revealing the diminished amplitude at very small orbital separations. The solid blue line shows the maximum relative amplitude of the differential signal (from a shifted copy of itself) of a PHOENIX-ACES spectrum with $T_{\text{eff}}=2500$ K, $\log g=5.0$, $[\text{Fe}/\text{H}]=0.0$ in the wavelength region 2110–2123 nm. The maximum difference is normalized by the median amplitude between $\pm 7\text{--}10 \text{ km s}^{-1}$, representing a complete line separation. The orange (dashed) and green (dot-dashed) lines represent the relative amplitude of a spectrum differential for a spectrum containing a single Gaussian or Lorentzian absorption line respectively, each with a unitary amplitude and a $\text{FWHM} = \lambda/R$. The solid vertical lines indicate the estimated companion ΔRV in these observations while the dashed vertical lines indicate the RV corresponding to the FWHM at this wavelength and resolution.

The vertical dotted lines indicate the line $\text{FWHM} = \lambda/R = v/c$ with a velocity of 6 km s^{-1} at $2 \mu\text{m}$ with $R=50\,000$, showing that the amplitude is almost maximum when the lines are separated beyond their line width. The two solid vertical lines in Figure 6.2 indicate the $\Delta RV=1.41 \text{ km s}^{-1}$ separation calculated for our best target, HD 30501 from Table 6.4, given known orbital parameters and the observation times. This shows that our differentials have severely reduced amplitude, $< 20\%$ relative to well separated individual lines. As the companion spectra are already faint and in combination with a host star at $>1\%$ flux ratio the $>80\%$ extra reduction in signal amplitude makes this detection impossible with these observations.

6.5 Orbital Solutions

The insufficient observational spacing becomes clear when the orbits are visualized by plotting the RV variation. Figures 6.3 to 6.11 show the RV curves for each target observed for this project. The target stars that have two companions are shown twice, with each companion treated as a single Keplerian (ignoring the presence of the other companion). For each figure the left hand plot shows the RV variation

across a full orbit of the companion, while the plot on the right shows the RV variation for the 6 month observation window of Period 89 only. The solid black line indicates the RV of the host star (with scale on the left hand axis), while the blue dashed line shows the RV of the companion (with the scale on the right hand axis). The orange crosses and red stars indicate on the RV curves the times at which observations were obtained for each target, for the host and companion respectively.

The first thing that is apparent is the variation of shape of the RV curves. This is normal with the variations in shape arise from the different orbital parameters of each target (provided in Table 6.2). In the left hand plots, in which a full orbit is shown, the different shapes are created from the eccentricity, e , and argument of periapsis, ω . In the right hand panels, for which a fixed time period is shown, the orbital period of the companion also plays a role. Specifically the ratio of orbital period to the 6 month observing period determines what fraction (or multiples) of the orbit is displayed.

The RV curves of the star and the planet mirror each other about the systems mean velocity, γ , with the amplitude scaled by their mass ratio, q (see Equation 2.14), and ω offset by 180° .

All the plots, apart from HD 4747, have more than one observations shown, although it can be difficult to see as there observational spacing is small.

For the companions HD 162020b (Figure 6.4) and HD 168443b (Figure 6.6) their orbital periods are shorter than 6 months, allowing for multiple orbits to occur during Period 89. As such the full amplitude range was available to measure in the observing Period if observations were taken at correct times, at the locations of the extrema. It should have been possible to obtain observations in which the companion spectra were sufficiently separated for the differential separation technique. However in reality, the two observations for these two targets were taken immediately after each other, making any differential extremely small. This is ignoring the fact that the flux ratios (from Table 4.4) for these short period companions are estimated to be very low, meaning they would have been very difficult to detect even if observed at the extrema.

The larger companion HD 168443c in Figure 6.7 has a longer orbital period, so it appears as straight line in the right hand panel, although the amplitude variation of the companion during Period 89 is about $8\text{--}9\text{ km s}^{-1}$. Therefore observations taken at the extreme ends of Period 89 may have provided just enough separation to be suitable for the differential.

For HD 202206 about 3/4 of the orbit is covered in Period 89 with a RV amplitude of the companion possible of over 40 km s^{-1} . Therefore, in this case well separated RVs could have been obtained.

For the remaining targets with long periods, it is clear that sufficiently separated RVs were not obtained, but also that they were not possible within a single observing period with a RV variation less than 6 km s^{-1} during Period 89. For HD 30501 the largest time separation between observations obtained is clearly visible in Figure 6.11. Unfortunately, this did not result in a large enough companion separation. Looking at the full period, if the observations had been obtained in the previous period then sufficient separation could have possibly been obtained.

The code used to create orbital plots similar to those shown here is available under the iastropt/Observationtools *GitHub* repository with documentation available on Read the Docs.

The sampling of points in the orbit reveal that the choice of points was not favourable for the application of the direct subtraction technique. This was unfortunately discovered after attempting to apply the technique.

change RV
scale for
hd4747 orbit

Fix plot titles

Check M2sini
labels - can we
get M2 only for
those that we
know

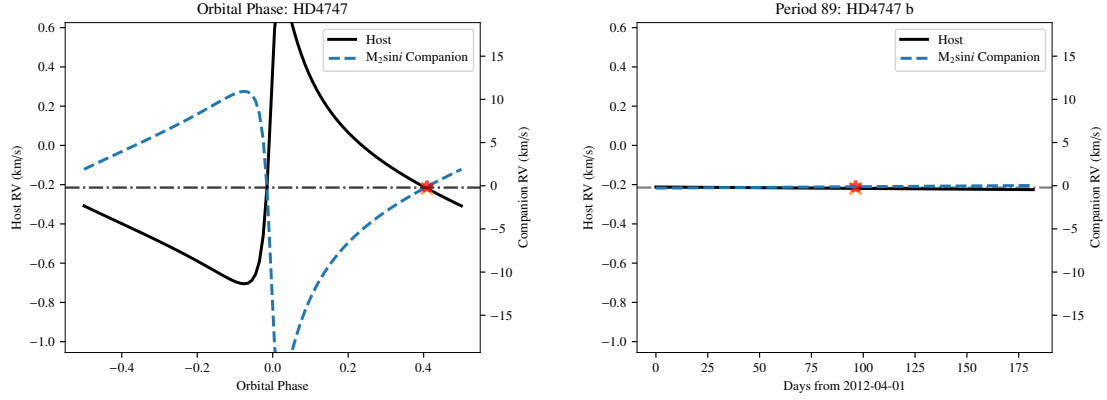


Figure 6.3: RV single companion Keplerian orbit for HD 4747. The left hand plot shows the RV curve for one full orbit while the right hand panel shows the RV curve over 6 months (Period 89). The solid black line indicates the RV of the host star (with scale on the left), while the blue dashed line indicates the RV of the companion (with scale on the right axis). The orange crosses and red stars indicate the times at which observations were obtained for the target, for the host and companion respectively.

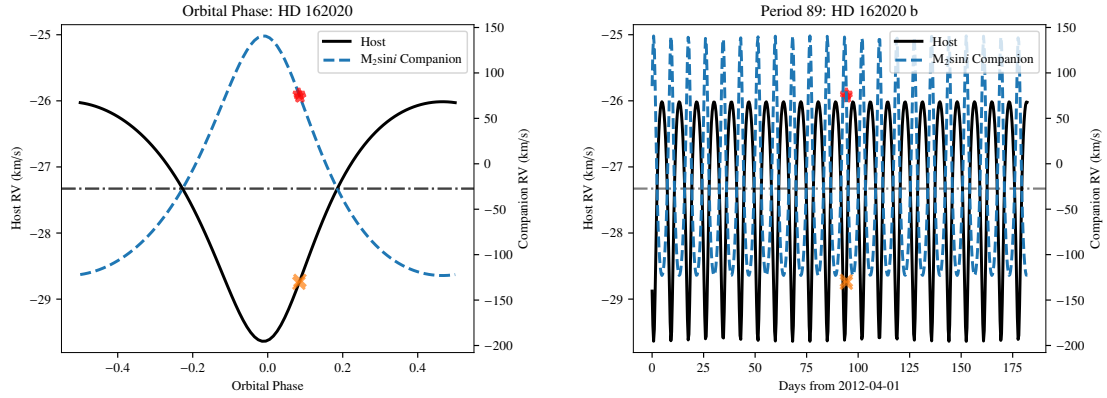


Figure 6.4: Same as Figure 6.3 but for HD 162020.

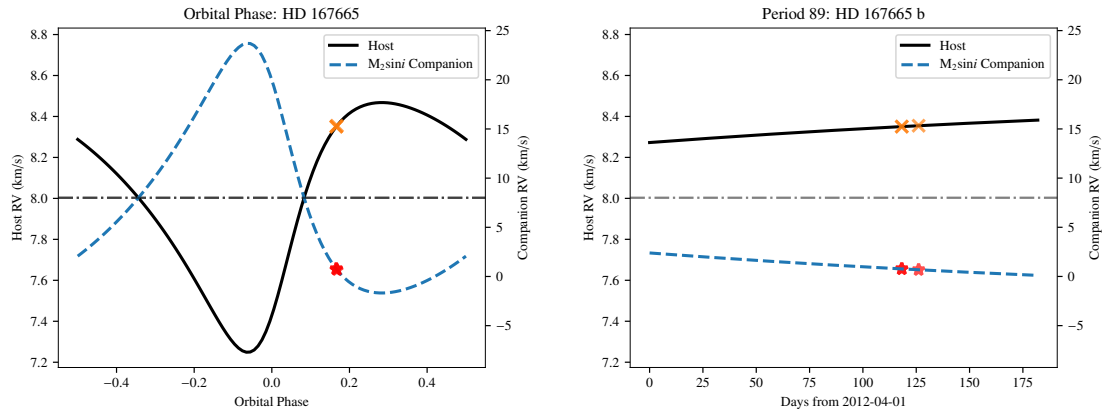


Figure 6.5: Same as Figure 6.3 but for HD 167665.

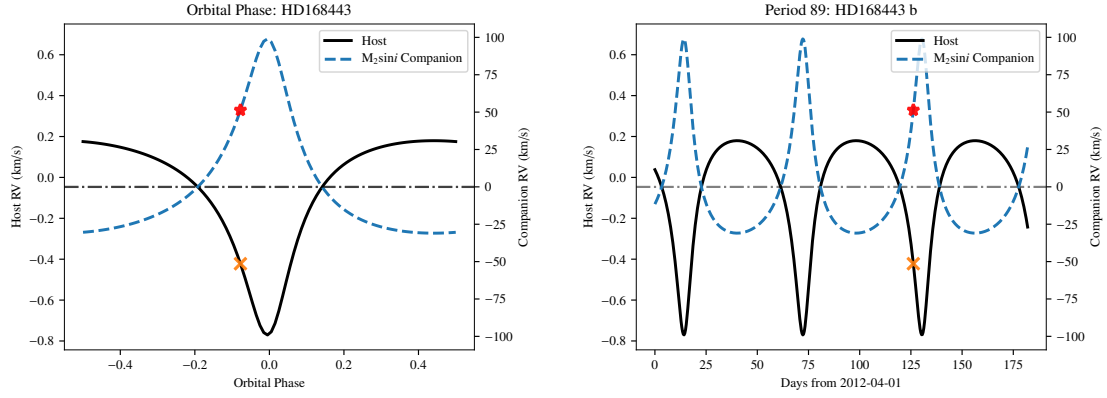


Figure 6.6: Same as Figure 6.3 but for HD 168443b. Analysed as if this was a single companion.

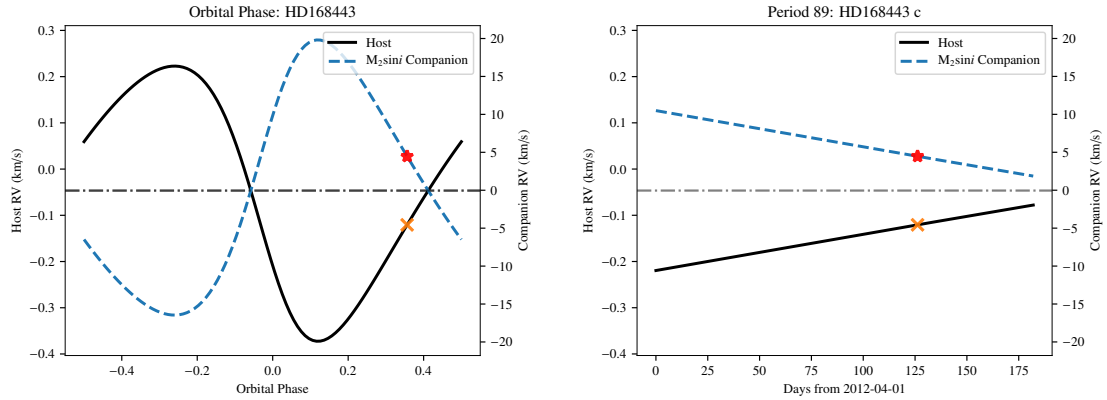


Figure 6.7: Same as Figure 6.3 but for HD 168443c. Analysed as if this was a single companion.

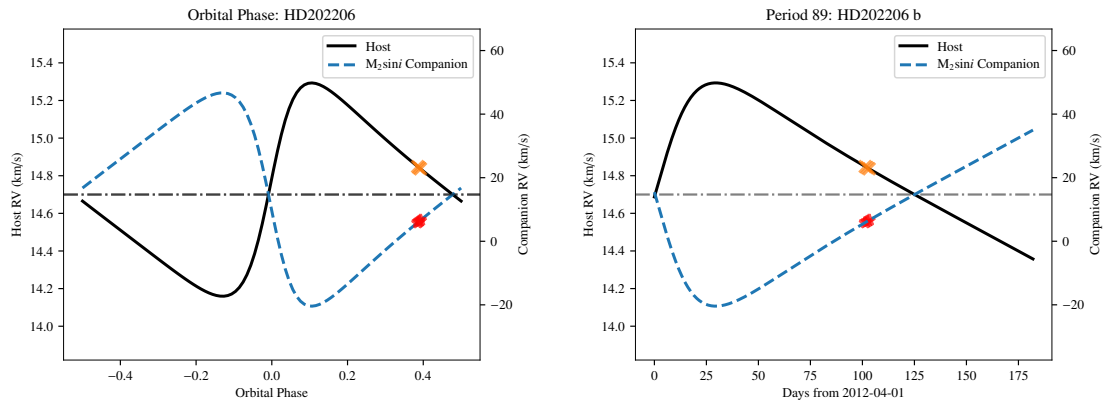


Figure 6.8: Same as Figure 6.3 but for HD 202206B. Analysed as if this was a single companion.

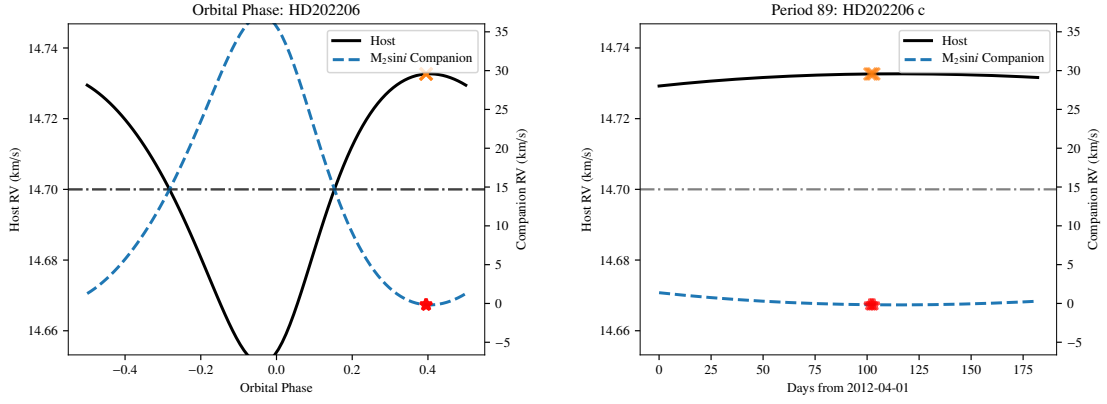


Figure 6.9: Same as Figure 6.3 but for HD 202206c. Analysed as if this was a single companion.

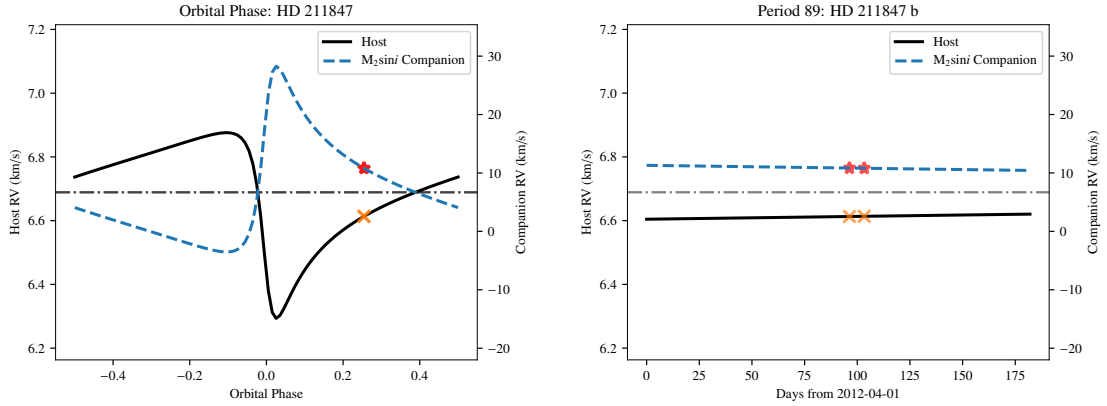


Figure 6.10: Same as Figure 6.3 but for HD 211847.

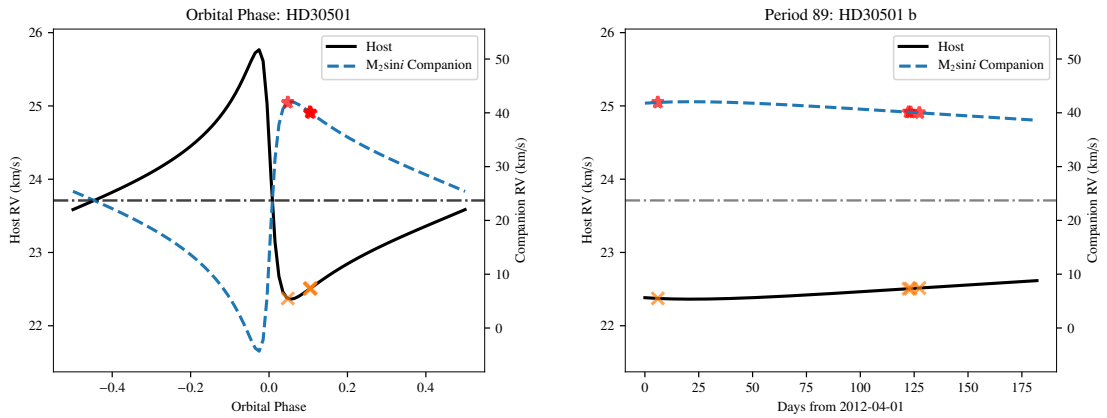


Figure 6.11: Same as Figure 6.3 but for HD 30501.

Should RV of companion be scale by $m_2 \sin i$ only or m_2 if known?

6.5.0.1 Differential scheduling challenges

This work has revealed that care needs to be taken in planning the observations for the application of the spectral differential technique of faint companions in the future. Future attempts need to pay attention in particular to: the FWHM of the lines in the region (governed by resolution and wavelength), the estimated companion separation ΔRV_2 ; and the previous observations from different observing periods, all while **and** keeping the detector settings consistent.

The original goal for the observations was to obtain two different and “clearly separated radial-velocities” for the secondary companion. However, the program was assigned a low-priority (C, in ESO grading) and, possibly due to operational reasons, the original time requirements necessary to secure well separated RVs for the companion spectra could not be met. This meant that all observations were insufficiently separated to extract a differential spectra for the companion.

The long orbital periods of these targets is also a strong contributing factor to the insufficient separations. Most of the targets observed here have orbital periods much longer than an observing semester (183 days). An optimal pair of observations (achieved at the extrema) would need to have been obtained from separate observing periods (between 2 months and 19 years apart). In some cases, even observations taken at the beginning and end of a single observing semester would not be sufficient to achieve a companion separation (depending on the phase and orbital parameters), requiring separate observing periods to even achieve the minimum ΔRV larger than the line FWHM. At the time (2012) it was impossible to ask for observation time over several semesters in a regular proposal.

This study demonstrates the importance of proposals for projects that need to be extended over several semesters or years. In the ESO context, this corresponds to “Monitoring proposals” (e.g. ESO, 2017, pg. 18). Observations of the targets explored here, with long orbital periods in particular, would benefit from the new abilities for multi-period proposals and scheduling systems which allow for tighter scheduling constraints, such as a companion RV separation.

For future observations in the context of the differential subtraction technique it is suggested that the best possible orbital solution of the host and companion be used to estimate the companions’ RV curve during the observing period, with the companion $M_2 \sin i$ providing an RV upper-limit. Radial velocity constraints are also valid for other studies such as the detection of reflected light from exoplanets **Martins et al., 2015**, e.g. Knowing the instrumental wavelength and resolution, an observing constraint can be set to avoid taking observations when the companion spectra are insufficiently separated, or the $\Delta RV_2 < \text{FWHM}$. This constraint can be set using the absolute and relative *time-link* constraints available in ESO’s Phase 2 Proposal Preparation (P2PP) tool. Additionally, analysing the known orbital solution beforehand to determine RV constraints will also help identify the best time to observe, if observations from separate periods will be required or, if an optimally separated companion differential is even feasible. Again the P2PP documentation for this observational proposal could not be obtained to check if these observations had used any of these features, which were available at the time, and set any constraints.

6.6 Contrast to other works

As stated previously the differential technique is not **new** being analytically formulated for binary star separation in Ferluga et al. (1997). This work tried to extend this to lower contrast ratios, to **a hosts**

with smaller companions.

For lack of high-resolution CRIRES data Kostogryz et al. (2013) explored simulations of the differential approach to a BD companion of a M-dwarf star, in which the contrast ratio is around 1/50 between 1/200 and were observed at the RV extrema. Their favourable wavelength choice to achieve a good contrast ratio is *K*-band, as done in work, however they chose the CO line region (~ 2310 nm) where there is several narrow spectral lines. One thing explored in Kostogryz et al. (2013) that is not considered here is the effect of rotational broadening on the mass determination, finding that it should be possible to determine the mass of a slowly rotating companion, but a fast rotating companion is more difficult.

The limitations with regards to the RV separation between spectral components has also been observed in other works. Similarly to the companion-companion RV separation focused on here, Kolbl et al. (2015) find a limitation of $\sim 10 \text{ km s}^{-1}$ RV separation required between the host and the companion. This is because if lines of the host and companion are blended, it is likely the companion spectra will be fitted, or incorporated into the hosts spectra, making it difficult to accurately detect the companions lines a similar RV. The RV difference between the host and companion is given in the last column of Table 6.3 as rv_2 . It can be seen HD 4747, HD 202206, and HD 218447 do not exceed this 10 km s^{-1} separation with the obtained observations.

6.7 Direct recovery in the mIR

It was investigated if this differential technique could be extended into the mid-infrared mIR domain. There were two reasons for this: to develop experience with the mIR domain where the contrast ratios are higher, and due to the lack of high-resolution nIR spectrographs available at the time (see Section 3.4).

VISIR is a mIR spectrograph on the VLT, offering diffraction-limited imaging at high sensitivity in three mid-infrared (mIR) atmospheric windows: the *M*-band at $5 \mu\text{m}$, the *N*-band between $8\text{--}13 \mu\text{m}$ and the *Q*-band between $17\text{--}20 \mu\text{m}$, respectively. The use of VISIR to detect the spectra of Brown Dwarf companions in the mIR was briefly explored. The candidate selected as the best target to investigate was HD 219828 which has a hot-Neptune ($M_2 \sin i = 21 M_{\oplus}$) (Melo et al., 2007) and a recently discovered super Jupiter ($M_2 \sin i = 15.1 M_{\text{Jup}}$) on a long period (13 yr) eccentric orbit ($e=0.81$) (Santos et al., 2016).

Based on the spectra of a cool brown dwarfs in the mIR, and the detector configuration available at the time, the best option for the observations was the low resolution mode covering the wavelength region $8\text{--}13 \mu\text{m}$. This wavelength region would have encompassed the NH_4 signature at $10.5 \mu\text{m}$ and the edge of a CH_4 band at $7.7 \mu\text{m}$, both large features in the BD mIR spectrum.

After performing flux ratio calculations between the host and companion using the Baraffe et al. (2003) models (see Section 4.4.1) and considering the performance of the VISIR instrument and the exposure time calculator it was determined that observations with VISIR to achieve a SNR of 100 were infeasible, requiring 1000's of hours of observing time to achieve the necessary signal-to-noise level to separate the companion from a blended spectra. For a different target, HD 189733 it was calculated that with an exposure time of 2 hours the SNR of the host and companion would be 85 and 4 respectively, using the low resolution spectroscopy mode. As such the direct separation approach was not explored further in the mIR.

6.8 Summary

This chapter presented the observations that were gathered having in mind the application of a differential subtraction method to recover the spectra of the faint BD companions. Due to the poorly separated observation times relative to the long orbital periods, the differential subtraction method presented in Section 6.3 was revealed to be inappropriate for these observations as the RV separation of the companion spectra between observations is significantly smaller than the width of individual spectral lines. The small separation of the companion causes the lines of the companion to also mutually cancel, severely reducing the residual signal to well below the available noise level. The requirement of well separated RVs for the companion spectra was clearly stated in the original proposal but was not satisfied by the observations, however the very large orbital periods of some of the targets would not produce a sufficient RV signal during one semester was possibly and oversight during the proposal stage. In the following chapter a different technique will be explored in the attempt to extract details of the companion from these observations which were insufficient to apply the differential.

Synthetic companion recovery

Following on from Chapter 6, in which the differential subtraction technique was unsuccessful due to the insufficient separation of the observations, a second method is attempted to detect the presence of the faint BD companions in the blended spectrum. In this chapter a χ^2 fitting approach is used to fit the observed spectra with a binary model comprised of two synthetic spectral components. An overview of the method is presented followed by the preparation of the models. A simulation with a larger M-dwarf companion to a G2V star is presented first, followed by a simulation and observations of HD 211847. Injection-recovery simulations are performed to understand the limitations of this method and the results obtained. A discussion of the results and a comparison to other similar techniques is given at the end.

7.1 Binary χ^2 spectral recovery

The approach developed here is to fit the observed CRIRES spectra, consisting of a FGK star with a BD companion, with a model comprised of a combination of two synthetic spectra, one for each component. This will be done using the χ^2 approach which has been extensively used in the literature (e.g. Astudillo-Defru et al., 2015; Passegger et al., 2016; Passegger et al., 2018; Zechmeister et al., 2018; Nemravová et al., 2016; Kolbl et al., 2015; Rajpurohit et al., 2018, to list a few). The recoverable information from the fitting will be the parameters of synthetic spectra fitted to the companion which will provide some indication of the companions temperature and spectral type, but it will not produce a direct mass constraint that was the original aim of the observations.

7.1.1 The χ^2 method

The well known χ^2 technique measures the weighted sum (for all data points i) of the squared deviation between the observation (O) and the computed models (C), with the minimum χ^2 value representing the best-fit parameters:

$$\chi^2 = \sum_i \frac{(O_i - C_i)^2}{\sigma_i^2},$$

where σ_i is the error on each measurement.

The inverse survival function of the χ^2 distribution is used to determine the confidence levels of the

resulting parameters from the minimum χ^2 . The inverse survival function returns a $\Delta\chi^2$ value from the minimum χ^2 value for a given σ level and degree of freedom. This can be achieved in *Python* with the *scipy* package as the single line of code `scipy.stats.chi2(dof).isf(1-p)`, where *dof* is the degree of freedom and *p* the probability; for example $p = 0.68$ for $1-\sigma$. For example, the $\Delta\chi^2$ for a single degree of freedom required for the $1-$, $2-$, and $3-\sigma$ confidence levels is 1, 4, and 9 respectively (Bevington et al., 2003). This method assumes that the measured flux is observed with a SNR sufficiently high so that the noise on the spectrum is approximately Gaussian, and the χ^2 method appropriate.

For a given observation, the χ_{red}^2 is computed as $\chi_{red}^2 = \chi^2/\nu$ where $\nu = n - m$, the number of observed pixels, n , minus the number of parameters of interest, m ¹. In the cases explored below the χ_{red}^2 is only calculated after **after** the summation across the detectors is performed.

For each observation O , the σ is estimated using the $\beta\sigma$ method (Czesla et al., 2018), using the MAD (median absolute deviation about the median) robust estimator. The $\beta\sigma$ method estimates the spectral noise of the spectra using a series of numerical derivatives². We followed the procedure outlined in Czesla et al. (2018) to analyse the results from successive parameter combinations to settle on an order of approximation (derivative level) of $N = 5$, and a jump parameter (pixels skipped to avoid correlations) of $j = 2$. The same σ value determined is applied to all points in the spectrum so that $\sigma_i = \sigma$. The $\beta\sigma$ method provides σ estimates for the target spectra which correspond inversely to SNR values between 100–400. These SNR values are similar to the values given in Table 6.3 which were calculated only using the standard deviation of the continuum of detector #2.

The computed models C are described in Section 7.1.2 and result in a multidimensional grid of χ^2 values for each combination of model parameters, namely the spectral parameters (e.g. T_{eff}), and the RV of the host and companion RV for each: detector, observation, and target.

The global minimum of the multidimensional χ^2 -space is used to represent the best fitting model combination to the observed spectra. The multidimensional χ^2 grid is summed across multiple detectors to also determine a global minimum χ^2 for the whole observation $\chi_{obs}^2 = \sum_{n=1}^N \chi_n^2$, where N is the number of detectors used. However, the separate observations are not combined as the RV parameters of the host and companion will vary between each observation³. To incorporate the separate observations a model that incorporates the phase information will be required and is beyond the scope of this work due to the limited number of observations (1–4). A promising method to incorporate the phase information for the detection of exoplanetary spectra is given by Lockwood et al. (2014) and Piskorz et al. (2016). They detect evidence of an exoplanet spectrum with an contrast of order 10^{-4} using nIR (L - and K -band) spectra with a $\text{SNR} \approx 2000$ observed at six epochs over the whole orbit.

7.1.2 Computed model spectra

In this section the transformation of the synthetic PHOENIX-ACES spectra into the computed models (C) is explained. These computed models will then be fit to the observed spectra.

Firstly, this assumes that the synthetic spectra are loaded and converted to consistent units. The loading is easily performed using Starfish’s GridTools (Czekala et al., 2015), which can load the library spectra with a list of stellar parameters [T_{eff} , $\log g$, $[\text{Fe}/\text{H}]$, $[\alpha/\text{Fe}]$]. The PHOENIX-ACES spectra are converted from the units of the spectral energy distribution ($\text{erg s}^{-1} \text{cm}^2 \text{cm}^{-1}$) (at the stellar surface)

¹ $m = 2$ or $m = 4$ in the examples explored below

² Applying a Taylor expansion to the spectra.

³ Since the current observations are insufficiently separated, it may be possible to combine the separate observations; but in general this would not be the case

into photon flux ($\text{photons s}^{-1} \text{cm}^2$) by dividing by the photon energy⁴. This can be simply achieved by multiplying the spectrum by the wavelength (multiplicative constants ignored), as done in Figueira et al. (2016). The spectra are also convolved with a Gaussian kernel to the instrumental resolution of the observations, in this case $R=50\,000$. Due to the distributive property⁵ of convolution the instrumental broadening is performed on each individual library spectrum first. This **it** to avoid performing convolution for each combination of model parameters in the binary model after the spectra have been combined. It would be more computationally expensive, **to** perform the convolution on every model combination, C .

These synthetic spectra are used individually for the single component model (Section 7.1.2.1) and also combined together into a binary model (Section 7.1.2.2). The results of these models are then interpolated to the wavelength grid of the observed spectra and the χ^2 calculated by comparing the model and observation at each wavelength point, i .

7.1.2.1 Single component model

The single component model C_i^1 comprises of a single synthetic spectrum, J , (with model parameters T_{eff} , $\log g$, $[\text{Fe}/\text{H}]$, $[\alpha/\text{Fe}]$ $[\alpha/\text{Fe}]$ that can be Doppler shifted by a RV value rv_1 .

$$C_i^1(\lambda) = J(\lambda_0(1 - \frac{rv_1}{c})) \quad (7.1)$$

where λ is the shifted wavelength, λ_0 , the model rest wavelength and, c , the speed of light in a vacuum. The model's flux in the wavelength region of the observations is continuum normalized to unity to match the observed spectra, and then interpolated to the wavelength grid of the observation.

This single component model analysis is similar to the Passegger et al. (2016) χ^2 fitting, using PHOENIX-ACES spectra to fit and determine the parameters of M-dwarf spectra. A similar re-normalization (see Section 7.1.3) as Passegger et al. (2016) is used to account for slight differences in the continuum level and possible linear trends between the normalized observation and models. However, unlike Passegger et al. (2016), no dynamical masking was applied to sensitive lines to make the χ^2 minima more distinct nor a linear interpolation of the stellar parameters between the grid models to obtain higher precision stellar parameters. This was because, at this stage, only the presence of the secondary is trying to be detected, not **determine** precise stellar parameters. These processes and others could however be included in the future to improve the detectability and precision of the best-fit model. Instead, a radial velocity component is included in the χ^2 fitting, which is not included in Passegger et al. (2016).

7.1.2.2 Binary model

In the binary model case the model is considered to be the superposition of two synthetic spectral components, one each for the host and companion respectively. Both components are Doppler shifted by rv_1 which represents the RV motion of the host star, while the companion spectra is also Doppler shifted by a second RV, rv_2 , representing the RV offset between of spectrum the host and companion. This choice is arbitrary⁶, but in this way the mean motion of the system relative to Earth is captured only in rv_1 . The two spectra are scaled by their radius squared (see Section 7.1.2.3) then added together, thus setting the relative amplitude of the two spectral components. Given two spectral components J_2

⁴ Photon energy $E = \frac{hc}{\lambda}$, where h , c and, λ are Plank's constant, the speed of light, and wavelength, respectively.

⁵ $I(\lambda) * (f(\lambda) + g(\lambda)) = I(\lambda) * f(\lambda) + I(\lambda) * g(\lambda)$

⁶ Having rv_2 as the companion RV offset from the rest wavelength is also a valid choice.

and J_2 with radii R_1, R_2 this equates to

$$C_i^2(\lambda) = J_2(\lambda_0(1 - \frac{rv_1}{c})) \times R_1^2 + J_2(\lambda_0(1 - \frac{rv_1}{c})(1 - \frac{rv_2}{c})) \times R_2^2 \quad (7.2)$$

The combined binary model is continuum normalized by dividing it by an exponential fitted to the continuum of the combined spectrum. Here at 2100 nm it assumed that the Rayleigh-Jeans regime is appropriate. This assumption is wavelength dependent and other continuum normalization techniques are may also be valid. In the case of a BD companion around an FGK star investigated here, the continuum is dominated by the contribution from the host star, contributing the majority of the spectrum with flux ratios below $\sim 1\%$, in the wavelength range 2110–2165 nm.

Models are combined in this way to represent the correct absolute flux ratio of the spectral components. A further method could allow a variable flux ratio to be included as an extra parameter and be fitted as well. However, it would add an extra dimension to the χ^2 grid and potentially add more degeneracy between models of the companion. The median flux ratio between the two components is calculated for the wavelength range used here as an indication of the flux ratio level. This is given as F_2/F_1 in Table 7.1

This binary model should provide meaningful information about the likely companion parameters (e.g. T_{eff}) and a possible estimate of the flux ratio of the system. These can be combined with the Baraffe et al. (2003) models to constrain the mass of the companion. However, care is needed with the binary model as the inclusion of extra spectral components and associated parameters could also provide a “better” fit to observations which have faint or even no companions, by fitting components of the noise.

The full list of grid parameters for the binary model are $T_{\text{eff}1}$, $\log g_1$, $[\text{Fe}/\text{H}]_1$, $[\alpha/\text{Fe}]_1$, rv_1 , $T_{\text{eff}2}$, $\log g_2$, $[\text{Fe}/\text{H}]_2$, $[\alpha/\text{Fe}]_2$, rv_2 where the subscripts 1 and 2 indicate the host and companion models respectively.

7.1.2.3 Effective radius

The PHOENIX-ACES spectra are calculated at the stellar surface. To combine the two synthetic spectra with the correct absolute flux ratio the stellar size needs to be accounted for. The emitted flux needs to be integrated over the effective surface area of each emitting body respectively. Ignoring the common multiplicative constants that will not affect the ratio between spectra and disappear with normalization the two synthetic spectra of the binary model are individually scaled by the square of their respective radii, R_1 and R_2 R_1 .

In this work the radius used to scale the spectra is the effective radius of each component from the PHOENIX model header; the PHXREFF keyword. This radius is utilized in the modelling of the PHOENIX-ACES stellar atmospheres. This is used as it is directly tied to each model spectrum, and already calculated and available. In this way it does not incorporate an extra assumption or model relating the library model parameters to a stellar radius. The ratio of the radii from the two synthetic spectra in the binary model examples presented are provided in Table 7.1 as R_1/R_2 .

Using the radii in this way for the companions has its limitations because as stated previously: there is a degeneracy in BD mass, age, and luminosity of the companion, and in particular a combination of radius-mass and radius-age relationships (Sorahana et al., 2013). Using the PHOENIX-ACES model effective radii does not allow for any independent age constraints to be incorporated into the stellar radius, or allow for any variability in the radii to account for uncertainties.

The targets analysed here do not transit, but in cases that did transit the radius ratio can be independently determined from the photometric transit method (Deeg, 1998). This independent radius ratio could be used as a constraint when combining the binary model spectra.

Radii of different parameters

7.1.3 Re-normalization

Slight trends in the continuum level between the observed spectra and computed models were removed using the re-normalization following Passegger et al. (2016):

$$F_{re-norm}^{obs} = F^{obs} \cdot \frac{\text{continuum fit}_{model}}{\text{continuum fit}_{observations}}. \quad (7.3)$$

The polynomial continuum fits to the normalized observations and models are used to re-normalize the observed spectrum to the continuum of the models. For detectors #1–3 a polynomial of first degree was used, while for detector #4 a polynomial of second degree was needed to fit the edge of a strong Hydrogen line (Brackett- γ) at 2166 nm, which lies just off of the edge of detector #4. This broad line is only observed in the synthetic spectra but not in the reduced observations. It is assumed that the edge of this line was normalized out during the reduction process.

For each model the continuum level is further allowed to be slightly varied by ± 0.05 as a free parameter taking the model that fits with the smallest χ^2 value as the choice for this combination of binary parameters.

7.1.4 Reducing dimensionality

The high dimensionality of the binary model makes it computationally challenging and difficult to analyse the χ^2 space. This section discusses the choices made to reduce the dimensionality and the parameter space, to reduce the computation time. For reference, the parameter space of the models is multiplicative. That is, each new dimension or parameter added multiplies the number of possible model combinations. When increasing from the single model to the binary model, the number of parameters doubles, but the number of possible models is actually squared, assuming that each spectral component can explore the full parameter space. The binary model is therefore more computationally expensive. In general the number of possible parameter combinations for k spectral components each with a grid of l models increases to k^l . If the full set of PHOENIX-ACES library spectra (66456) is explored with a binary fit then this naively balloons to over 4.4 billion possible combinations. This is the worst case scenario as half of these combinations are not unique as the host and companion components will be swapped. A number of assumptions are implemented to vastly reduce the parameter-space enabling faster computation.

The first assumption is to restrict the Alpha element abundance ($[\alpha/\text{Fe}]$) of the models to zero. This is likely a very good approximation as all the targets have solar metallicity and are thus very likely to belong to the thin disk of the Galaxy, where $[\alpha/\text{Fe}]$ values are close to zero, i.e. solar Adibekyan et al. (e.g. 2012). The second assumption is that the search space can be significantly reduced by using literature values of the host star given in Table 6.1. The metallicity of both model components are fixed to the closest grid to the literature value of the host star, usually $[\text{Fe}/\text{H}]=0.00$. The $\log g$ of the host star is also fixed to the closest grid literature value. The uncertainties on the literature measurements for $\log g$ (~ 0.1) and metallicity (~ 0.05) are both smaller than the grid steps of 0.5 for these parameters. For the

$\log g$ of the companion is obtained from the Baraffe et al. (2003) and Baraffe et al. (2015) evolutionary models for the given companions mass (M_2 or $M_2 \sin i$) and hosts age.

A starting point for $T_{\text{eff}2}$, the estimated companion temperature from the Baraffe evolutionary models is used, given the companion mass and stellar age. The temperature grid is extended about this value in each in each direction, within the temperature limits of the synthetic model limits. For example the companion temperature grid spans -600 to $+400$ K in Figure 7.1 and ± 400 K in Figures 7.2 and 7.3 about the estimated companion temperature.

The large number of possible combinations stated above also do not include the RV grid for each component, which is user defined and can have a variable resolution, and amplitude. For example for a fixed RV range a decrease in the grid step size (a finer RV resolution) the number of models to consider increases. The RV grid space can be reduced significantly by tailoring it to the target being examined. For each target and observation, the estimated RV values from Table 6.3 are used as a centre starting point for the rv_1 and rv_2 values and then incremented within a few FWHM around those values, or out to the targets K_1 or K_2 values.

An iterative process could potentially have be implemented to refine the RV grids, starting with a larger grid with lower RV resolution and then performing a higher resolution grid about the minimum χ^2 RV values. This was attempted manually during testing but it could be easily automated in the future, at the cost of recalculating the χ^2 at different RV resolutions. One could expect that a good starting RV grid step be governed by the spectral resolution, e.g. comparable to the FWHM velocity.

Also for the companions targets with a fully resolved orbit the known RV of the host star, rv_1 could also be held fixed, however this was not performed in this work.

7.2 Simulation and results

In this section some results from applying the models for companion recovery model to simulated observations and to the observed target with the best estimated contrast are presented.

7.2.1 Simulated binaries

To test the companion recovery method simulations of binary observations using PHOENIX-ACES spectra were performed. These are performed in the wavelength range between 2112–2152 nm, covering the first three detectors of CRIRES only, due to spectral mismatch observed later in the observed spectra. White noise was added to the simulated spectra a standard deviation $\sigma = 1/\text{SNR}$, for a given signal-to-noise (SNR) level. The χ^2 grid-search recovery technique detailed above is applied and the resulting parameters compared to the inputs.

The results of two example binary simulations are displayed in Figures 7.1 and 7.2, both simulated with a SNR of 150. In each figure the input and recovered parameters for the binary components are indicated by the red circles and yellow stars respectively, and are given in Table 7.1. The $3\text{-}\sigma$ contour is shown with a white line on the plots to indicate the shape of the confidence level only. The $1\text{-}\sigma$ contours are not shown here as they are much smaller than the temperature grid step and are difficult to visualize at this scale, often being smaller than the marker shown at the location of the minimum χ^2 . Each coloured rectangle is centred on a grid point, with its colour indicating the χ^2 value, and its shape indicating the resolution of the parameter grid space searched.

Table 7.1: Input and recovered parameters on simulations and an observation when applying a single (C^1) and binary (C^2) models. The $\log g$ and metallicity were fixed at values of $\log g_1 = 4.50$, $\log g_2 = 5.0$ and $[\text{Fe}/\text{H}]_1 = [\text{Fe}/\text{H}]_2 = 0.0$. Gaussian noise with a SNR of 150 was added to both simulations. The number of data points and parameters used in each model are m and n respectively.

	Simulation 1			Simulation 2			Observed HD 211847		
	Input	Recovered C^1	Recovered C^2	Input	Recovered C^1	Recovered C^2	Expected	Recovered C^1	Recovered C^2
$T_{\text{eff}1}$	5800	5800	5800	5700	5800	5700	5715 ± 24	5900	5800
$T_{\text{eff}2}$	4000	—	3800	3200	—	3100	~ 3200	—	$> 3800^a$
rv_1	0	0.1	0	6.6	6.6	6.6	6.6 ± 0.3	7	7.6
rv_2	10	—	9.8	0.5	—	-1	0.5 ± 2	—	-12.6
R_1/R_2	2.57	—	2.71	3.16	—	3.27	3.16	—	$< 2.71^a$
F_2/F_1	0.084	—	0.066	0.030	—	0.026	0.030	—	$> 0.066^a$
m	—	3072	3072	—	3072	3072	—	2612	2612
n	—	2	4	—	2	4	—	2	4
χ^2	—	4978	3792	—	3746	3630	—	37 688	33 860
χ_{red}^2	—	1.62	1.24	—	1.22	1.18	—	21.3	19.2
BIC	—	-20 145	-22 315	—	-21 477	-21 377	—	18 281	14 468

^a At the arbitrary upper limit for companion temperature grid (3800 K).

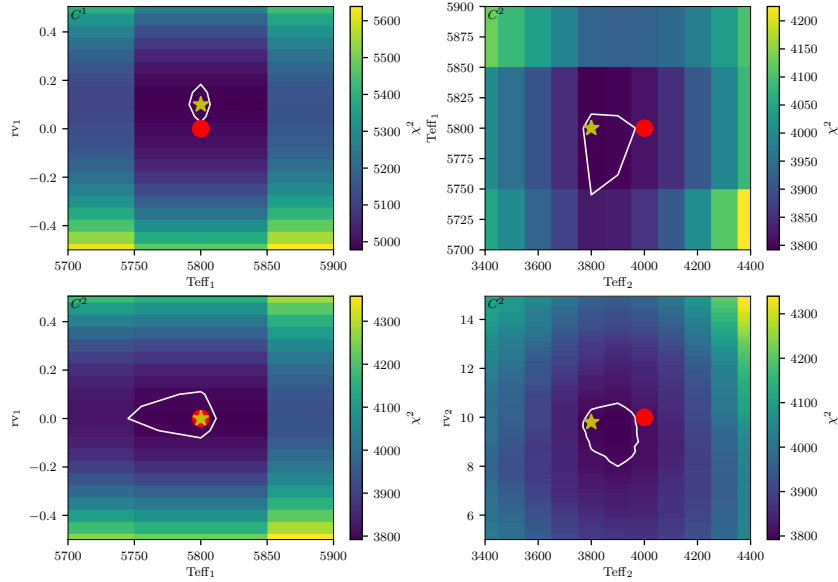


Figure 7.1: χ^2 results for companion recovery of a simulated binary observation of a Sun-like star ($T_{\text{eff}1} = 5800 \text{ K}$) with an M-dwarf companion ($T_{\text{eff}2} = 4000 \text{ K}$). The top right plot shows the application of a single component model (C^1) while the other three are using a binary model (C^2). Both left hand panels show the distribution of host temperature and host RV. The top right panel shows the distribution for host and companion temperature, and the bottom right the companion temperature and radial velocity. The red circle and yellow star indicate the location of the simulation input and recovered parameters respectively. The white line shows a $3\text{-}\sigma$ confidence level about the minimum χ^2 solution grid point. Each box is centred on the parameter values and shows the grid resolution.

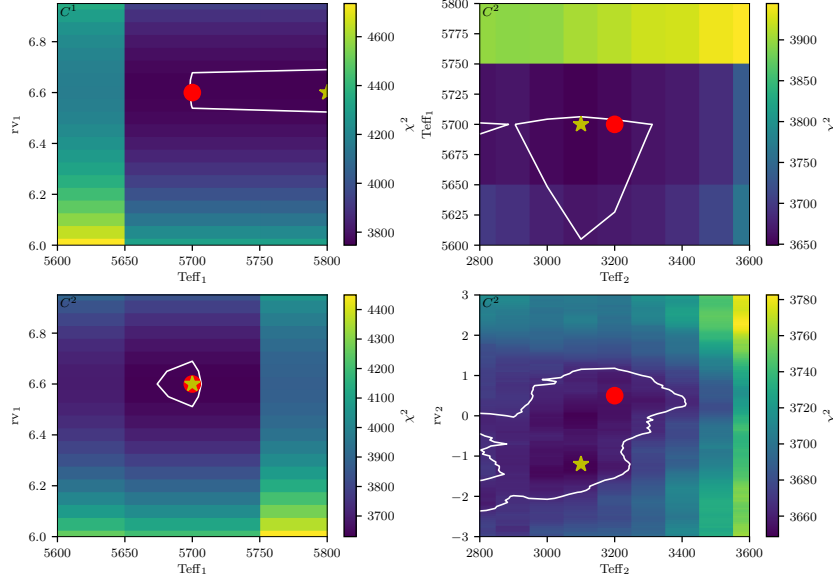


Figure 7.2: χ^2 results for companion recovery of a simulated binary observation similar to HD 211847, $T_{\text{eff}1} = 5800$ K, $T_{\text{eff}2} = 3200$ K, similar to Figure 7.1.

M-dwarf companion

The first simulation is for a Sun-like star with a M-dwarf companion with temperatures $T_{\text{eff}1} = 5800$ K, $T_{\text{eff}2} = 4000$ K. The results are shown in Figure 7.1. The top-left panel shows the recovered host parameters when only the single model is fitted to the spectra of the simulated binary. The top-right and both bottom panels show different parameter slices recovered when fitting with the binary model. Both left-hand panels display the parameters for the host, $T_{\text{eff}1}$ and rv_1 , to easily compare between the two models. With both models the host temperature $T_{\text{eff}1}$ is exactly recovered. The recovered host RV, rv_1 , is 0.1 km s^{-1} (two grid spaces) different from the input value in the single component model and is correctly recovered with the binary model.

For the companion the minimum χ^2 location for the companion temperature is 200 K below the simulated value, and the RV of the companion recovered is 0.2 km s^{-1} below the input value. The input values for the companion are just outside of the $3\text{-}\sigma$ contours shown. The flux ratio for the input is 0.08 while the flux ratio recovered is 0.066 . This begins to show the difficulty of recovering the companion.

HD 211847 simulation

A second simulation is performed with parameters to mimic the observation of the target with highest flux ratio, HD 211847, and is shown in Figure 7.2. In this simulation the single component model recovers a host with the correct RV but a temperature 100 K higher than the input value (one grid step). Again, adding the companion with the binary model recovers the correct host temperature. The companion temperature recovered is 100 K lower than the input temperature and the RV is different by 2 km s^{-1} which is around one third the FWHM.

In this case with a companion RV offset, rv_2 , near 0 km s^{-1} the host and companion lines are blended. The same spectral lines from both components are trying to match the same features of the spectra, making it more difficult to recover the companion parameters. In the bottom right panel there appears

to be multiple minima for different rv_2 and $T_{\text{eff}2}$ combinations, with a complex $3\text{-}\sigma$ confidence contour. This is assumed to be partially due to the small rv_2 .

From the result **summary** in Table 7.1, both simulations have a χ^2_{red} for the binary model closer to 1 than the single model. This is not surprising as the binary model contains extra parameters. As mentioned above, care is needed, as the extra components from the binary may just happen to fit components of the noise when a binary is not present, or at **a** extreme low contrast ratio as in this case. To further analyse the significance between the two models the ‘‘Bayesian Information Criterion’’ (BIC) (Schwarz, 1978) is used:

$$BIC = n \ln(m) - 2 \ln(\hat{L}). \quad (7.4)$$

Here n and m are the number of parameters and number of data points respectively and \hat{L} is the maximum of the Gaussian likely-hood function,

$$\hat{L} = \left(\frac{1}{\sigma\sqrt{2\pi}} \right)^m \exp\left(-\frac{\chi^2}{2}\right), \quad (7.5)$$

written in terms of χ^2 and a fixed σ for all data points. The maximum likely-hood of a Gaussian distribution is equivalent to minimizing the χ^2 . In both simulations the change in BIC between models, **$\Delta BIC > 10$** , so the preference of the binary model, with the lower BIC value, over the single component model is considered *significant*.

7.2.2 HD211847 observation

HD 211847 is the best candidate of the current targets for companion detection with the χ^2 binary model as it has a $155 M_{\text{Jup}}$ low-mass star companion Moutou et al. (2017). Even though it has been determined not a BD in the literature it has the highest estimated flux ratio out of the current sample, of 0.03 based on the Baraffe et al. (2015) evolution models and the known companion mass (see Table 4.4). Moutou et al. (2017) used Angular Differential Imaging **ADI** with SPHERE@VLT to observe an angular separation of the two bodies of 219.6 mas corresponding to a projected separation of 11.3 au. For comparison the CRIRES slit **with on the sky** is 400 mas. However, it was not determined if the orientation of the orbit was considered during the observation, to align the slit along the orbit. The result of applying χ^2 fitting to the second observation of HD 211847 is given in Table 7.1 and visualized in Figure 7.3.

For the fitting of this target the metallicity of both components was fixed to 0.0 and the $\log g$ for the host was fixed at 4.5. The $\log g$ for the companion is also fixed to 5.0, based on the Baraffe et al. (2015) evolutionary models for the given companion mass and system age. The orbital solution of the target was used to define the initial RV search space of both components, however the first range for the companion RV was too narrow and was extended until the companion was recovered with a value inside the RV bounds.

Again the top left panel of Figure 7.3 shows the recovery with a single component model with the other three displaying parameter slices of the binary model. Here the red circle marks the location of the expected values from the literature while the yellow star indicate the location of the minimum χ^2 recovered parameters. The **error** bar on the host temperature also comes from the literature, while the error on estimated RV values, shown in Figure 7.3, is calculated by applying the general error propagation formula (Ku, 1966) to the RV equation (Equation 2.12) and using the errors on the published orbital

parameters. For a function, f , with errors on the inputs δx , δy etc., it follows:

$$f = f(x, y, z, \dots) \quad (7.6)$$

$$\delta f = \sqrt{\left(\frac{\partial f}{\partial x} \delta x\right)^2 + \left(\frac{\partial f}{\partial y} \delta y\right)^2 + \left(\frac{\partial f}{\partial z} \delta z\right)^2 + \dots} \quad (7.7)$$

The fitted single component model finds a temperature of 5900 K for the host with a rv_1 of 7 km s^{-1} . This is 200 K and 0.4 km s^{-1} different above the expected parameters. The binary model finds a host temperature of 5800 K, which is the second closest model to the literature value, <100 K different. The host RV value recovered with the binary model is 7.6 km s^{-1} , which is 1 km s^{-1} higher than expected, but again these RV differences are smaller than the FWHM of the lines. For the single component model there is a barely noticeable evidence of a secondary minima near this 7.6 km s^{-1} RV value which is recovered by the binary model. The $3\text{-}\sigma$ contour in these plots is small due to the large gradient of the χ^2 , it is just visible on the right hand side of the star in the bottom left panel, and hidden behind the markers in the other panels.

For the companion in the binary model, on the right side of Figure 7.3 shows a problem. The minimum χ^2 for the companion temperature is at the upper limit of the grid shown. If the grid is extended the companion temperature towards higher temperatures the best fit location continues to increase in the recovered temperature, continually hitting the upper limit until it is close to the host temperature, more than 2000 K above the expected companion temperature. When the companion temperature becomes this high it also affects the recovered parameters for the host star to offset the features of the brighter companion. Also the companion RV is $>12 \text{ km s}^{-1}$ different than the expected value, around two line FWHMs away. Obviously this is not correct and the actual companion is not being detected.

The χ^2_{red} values for the single and binary models are 21 and 19 respectively, far from the value of 1, indicating that both models are a poor fit to the observations. The $\Delta BIC = 3812 > 10$ indicating that the binary model is preferred, i.e. the difference is *significant*.

The spectrum of the best fit solution binary model is shown against the observed spectra in Figure 7.4. It is observed that there is a large spectral mismatch between the synthetic models and the observed spectra. Extra wavelength masking was applied to many of the largest mismatched synthetic lines to remove their influence on the χ^2 . The grey areas mark regions which have been masked out, either from the centres of deep telluric lines (the thin masks matching spectral gaps), or the more prominent mismatched lines in the synthetic spectrum excluded from the χ^2 analysis. One clear example of a mismatched line is a synthetic line at 2132.5 nm that is clearly not observed in detector #2 (top right). Even with the majority of the mismatched lines removed the detection of the companion was still unsuccessful. The shown results for the observed spectra include the wavelength masking.

For detectors #1 and #2 it appears that the synthetic spectra contain many more deeper lines than observed. For detector #3 the red half of the detector was masked out as there appears to be an RV offset between the observed lines and synthetic spectra. With 3–4 lines that appear to be consistently offset from the observation it could be a wavelength calibration issue, although the telluric lines appear to be sufficiently corrected in this region, attesting for the quality of the wavelength calibration, and making it incompatible with the offset.

For detector #4 the observed lines do not agree at all with the models. With many observed lines not in the model and only one line with some agreement in wavelength, detector #4 is masked out completely

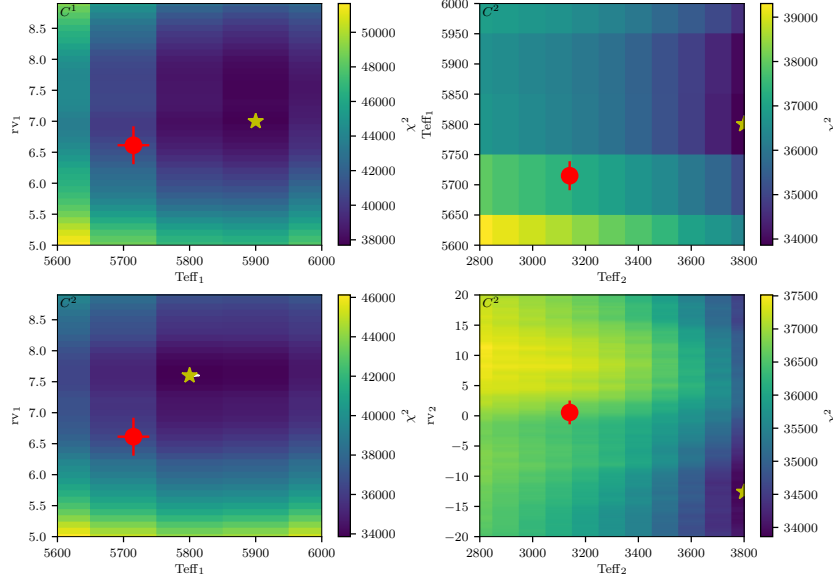


Figure 7.3: χ^2 result grid for the second observation of HD 211847, similar to Figures 7.1 and 7.2. The white line shows a $3\text{-}\sigma$ confidence level about the minimum χ^2 solution grid point, not always visible here due to the large χ^2 values. The error bar on $T_{\text{eff}1}$ is from the literature while the error bars on rv_1 and rv_2 are calculated by propagating the orbital parameter uncertainties through the radial velocity equation (Equation 1.1).

and not used in the χ^2 fit of the simulation or observed spectral fitting. Individual inspection of the χ^2 results for each detector also revealed that there was a large discrepancy between the 4th detector and the other three, with a different RV value for the host star and χ^2 values an order of magnitude higher. The edge of a deep Hydrogen line (Brackett- γ) off the edge of the detector #4 is also clearly seen in the continuum of the model $>2162\text{ nm}$, and possibly part of the reason for the poor fitting.

The same method was applied to the remaining targets, all with similar results for the companion, having companion spectra well above the expected values. In brief, it is concluded that the companion spectra cannot be correctly detected in the observation presented here using this method.

7.2.3 Companion injection-recovery

To determine the detection limits for this method an injection-recovery approach was used to simulate spectra with a range of companions. This is done by using the observed spectra and injecting onto them a synthetic companion, at the absolute flux ratio to which it would have been added to a synthetic host with the same parameters. The RV of injected companion is set to 100 km s^{-1} so that the companion lines are well separated from the lines of the host. This separation chosen is slightly larger than the largest host-companion separation (HD 162020) in the observed targets, given in Table 6.3 rv_2 .

The search space for the injection-recovery is restricted by fixing the host parameters $T_{\text{eff}1}$ and $\log g_1$ to those recovered fitting the non-injected spectra by a single component model. This leaves only the companion $T_{\text{eff}2}$ and rv_2 parameters free, to recover the injected companion. The wavelength masking is used to reduce the level of mismatch between synthetic and the observed spectra. The spectra were injected with companions between $2500\text{--}5000\text{ K}$ and the companion recovery attempted on each.

The injection recovery also performed on a synthetic host spectra representing each target as a

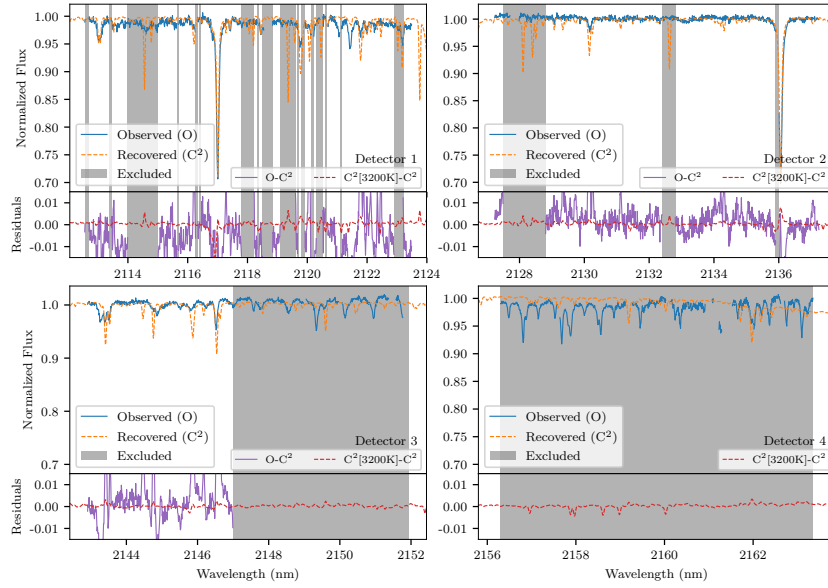


Figure 7.4: Comparison between the observed HD 211847 spectrum (blue) and the best fit synthetic binary model (orange dashed) for each detector. The bottom section of each panel shows the residuals between the parts of the observation used in the χ^2 fit and recovered binary model ($O - C^2$) in purple. The red dashed line shows the difference between the recovered binary model and the binary model with the exact same parameters except for the estimated companion temperature of 3200 K ($C^2[3200K] - C^2$). The grey shading indicated the wavelength regions where masking has been applied. The thinner masked regions that match with cuts in the observed spectra are where the centres of deep ($>5\%$) telluric lines that have been masked out are.

Table 7.2: Upper mass limits of target companions assuming a companion $\log g=5.0$. Masses are derived from Baraffe et al. (2015) evolutionary models using T_{eff} and $\log g$. The flux ratio F_2/F_1 is the absolute flux ratio between the cut-off temperature and the target host star.

Target	T_{eff} cut-off (K)	F_2/F_1	Mass limit (M_{Jup})
HD 4747	3900	0.084	598
HD 162020	3900	0.147	598
HD 167665	3800	0.054	560
HD 168443	4000	0.094	618
HD 202206	3900	0.075	598
HD 211847	3900	0.079	598
HD 30501	3800 ^a	0.106	560

^a From observed spectra

comparison. For the synthetic host injection-recovery the wavelength range of the synthetic spectra used is three sections interpolated to 1024 values in the wavelength span of detectors #1, #2, and #3. For each section, Gaussian noise is added at the level measured in the corresponding detector in the observation of the target being represented.

In Figure 7.5 the results of the injection-recovery on HD 30501 **are** show the injected companion temperature verses the companion temperature recovered. The blue dots represent the injection into the real observations, while the orange triangles represent injection into the synthetic host. Error bars of ± 100 K are included to indicate the temperature grid size only, and do not come from the recovery itself. The black dashed diagonal is the temperature 1:1 relation, where a correctly recovered companion should reside.

The grey shaded region indicates the ± 1000 K temperature range explored for the injection-recovery of the companion. This shows how the bounds of the grid can be recovered at low companion temperatures and that the recovered temperature deviates from the injected companion temperature around 3800.

For HD 30501 the injection onto synthetic and observed spectra produce similar results. At temperatures above 3800 K, in both the real and synthetic spectra, the injected companion is recovered within 100 K. For injected companion temperatures below 3800 K the temperature recovered is systematically higher than the injected value. This indicates that the companion is not correctly recovered and is affected by the added noise. The temperature of deviation is deemed to be the upper temperature limit for the recovery by this method. For the other stars **upper** limit from the injected observations could not be reliably determined, mainly due to spectral mismatch issues. In these cases the results from the synthetic injection are used to derive a temperature recovery cut-off for each target, each simulated with the closest synthetic spectrum to the host star.

Using the temperature cut-off values, an upper mass limit is derived for the companions around our stars using the Baraffe et al. (2015) evolutionary models, finding the closest point matching the spectral temperature cut-off and $\log g = 5.0$. These values are given in Table 7.2 and are between 560–618 M_{Jup} . The flux ratio between the cut-off companion spectra and the host star are also calculated, being between 5–15% in this wavelength span.

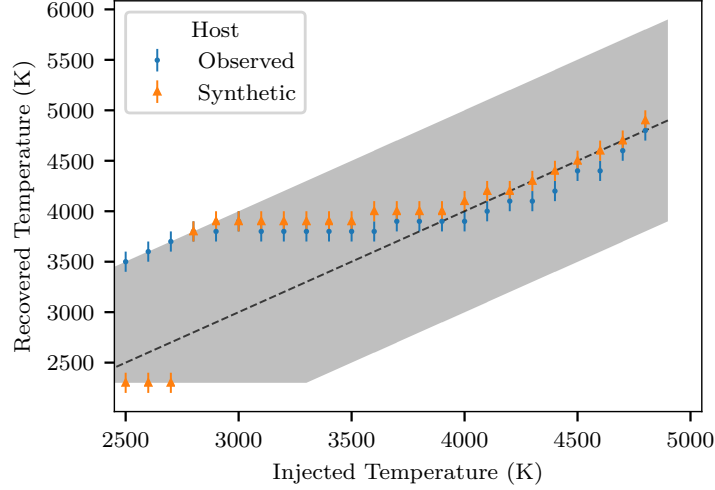


Figure 7.5: Result of simulated injection-recovery of synthetic companions on HD 30501. The blue dots and orange triangles indicate the recovered companion temperature for the observed and synthetic spectra respectively. The ± 100 K error bars are the grid step of the synthetic models. The black dashed diagonal shows the 1:1 temperature relation. The grey shaded region indicates the ± 1000 K temperature range explored. Gaussian noise added to the synthetic spectra was derived from the observed spectra.

7.3 Discussion

The spectral differential and the synthetic recovery methods attempted both in this chapter and Chapter 6 were both unsuccessful in an actual detection of the BD companions focused in this work. The injection-recovery simulations at a SNR of 300 give a companion upper mass limit around 600^{+20}_{-40} , above which this method detects a simulated secondary spectra. This is very high, roughly six times higher than the BD mass limit $\sim 80\text{--}90 M_{\text{Jup}}$. Some potential reasons and solutions for these poor results are given below, that hopefully can provide some guidance for any future attempts with these methods.

7.3.1 Mismatch in synthetic models

It is believed that spectral mismatch between the observation and synthetic spectra is the main cause of the unsuccessful companion detection, impacting the recovery in two ways. The mismatch causes the χ^2 values to be large in general, but this also causes the companion temperature to be pushed to higher temperatures in the application to the real observations.

In the examples shown the $\log g$ and metallicity of the synthetic models are held fixed, leaving only temperature to vary. The temperature impacts the synthetic spectral models in two main ways: the flux level of the continuum, and the number and strength of the absorption lines. In the binary model the contributions of the individual components is scaled by the flux ratio. If the temperature of the companion increases then the flux and radius of the companion increases and the flux ratio F_1/F_2 decreases. This effectively makes the lines in the host component relatively smaller in the normalized binary model spectrum. Due to the large initial mismatch of synthetic spectral lines of the host, a decrease in the relative strength of the host lines reduces the χ^2 value. This causes the recovered temperature of the companion to be higher than expected, >2000 K higher if allowed by the size of the exploration grid. The χ^2 approach is dominated by reducing the mismatch in the spectrum of the host rather than detecting

the spectra of the companion. This spectral mismatch is not observed in the simulations in Section 7.2.1 because they are created using the synthetic spectra themselves, and hence they do not have this same problem with the companion temperature.

Although the newer generations synthetic spectral models are improving and match the overall spectral energy distribution reasonably well there are still regions in the H - and K -band where there is room for improvement (Rajpurohit et al. (2016)). These can come in several forms, such as molecular line lists, abundance measurements, or further modelling. As one example in particular, Rajpurohit et al. (2016) previously inferred that the TiO line list poorly matches the real positions of TiO lines at spectral resolutions of $\sim 100\,000$. Passegger et al. (2018) has also noted inconsistencies in the line depth of synthetic spectra. The spectral mismatch in the region studied here is still too large for spectral recovery of companion brown dwarfs. In the nIR there is a compounding problem: the model input physics of sub-stellar temperatures and chemistry combined with the general difficulty of the nIR.

Find the wavelengths of some missing lines in the Mismatch, what elements do they belong to

7.3.2 Line contribution of faint companions

One thing easy to overlook when attempting to detect the binary companion at low flux ratios is the actual contribution of the spectral lines of the companion. Here the line depths in the synthetic companion spectra are calculated to determine the SNR levels required to detect the lines of the binary companions.

The flux ratio of the continuum for the most promising target analysed here is $F_2/F_1 \sim 3\%$ with the other targets having an expected flux ratio below 1%. The spectral lines of the individual components, which are the features that allow the identification and recovery of the components, have depths on average around 10–20% of their respective continua; at least between 2110–2160 nm. In effect, the companion line features have a depth $\ll 1\%$ relative to the continuum of the combined spectrum.

In Table 7.3 some properties of the spectral lines in the PHOENIX-ACES library between 2110–2160 nm are calculated. The number of spectral lines (*no. lines*) deeper than 5% are counted and the the average depth (*avg. depth*) of these lines is calculated. The contribution depth *cont. depth* of the companion lines to a combined spectrum is calculated to account for the flux ratio between the two spectral components. Here a Sun-like host with $T_{\text{eff}1} = 5800$ K is used for the comparison. This simplified combination neglects the continuum shapes of both spectral components and uses the average flux ratios for this wavelength range. The PHOENIX-ACES spectra in the temperature range of 2500–5000 K shown in Figure 7.7 can be used to get a visual indication of the line density and depth measured here.

For the lower temperature spectra there are more lines $>5\%$ deep, with 360–460 lines in this wavelength range, compared with only 31 deep absorption lines found in a Sun-like spectrum in this range. The average line depth of these lines is also larger than the Sun-like spectrum, around twice as deep. However, when accounting for the flux ratio, the contribution of the companion lines is 1–2 orders of magnitude smaller than the lines of the host.

For example, with the synthetic model for the companion of HD 211847, the average contributions of lines $>5\%$ become only 0.3% deep in a binary with the Sun-like spectrum. For a companion with a temperature of 2300 K (the lower PHOENIX-ACES temperature limit) the deepest lines contribute lines only around 0.1%.

The SNR of the observed spectra is between 100–300, which is below the SNR of 323 needed for the detection of the low-mass star companion of HD 211847 with temperature of 3200 K and $\log g$ 5.0. For the other targets with BD companions at and below the PHOENIX-ACES temperature range, a

Table 7.3: Contribution of synthetic lines within 2110–2160 nm of synthetic PHOENIX-ACES spectra to a binary model. F_2/F_1 is the continuum flux ratio between a spectrum with the given T_{eff} and $\log g$ and a Sun-like spectrum with $T_{\text{eff}}=5800$, $\log g=4.5$ (right most column). *No. lines* is the number of spectral lines deeper than 5% from the continuum of the individual spectra while *avg. depth* is the mean depth of those lines. *Cont. depth* is the average contribution, or depth, of these lines in the combined spectrum of a binary with a Sun-like spectrum. The SNR is signal-to-noise level required to have Gaussian noise $\sigma = 1/\text{SNR}$ equal to the *cont. depth* level in the binary model. All synthetic spectra used here have $[\text{Fe}/\text{H}]=0.0$.

T_{eff} (K)	2300		3200		5 800 (F_1)
$\log g$	5.0	4.5	5.0	4.5	4.5
F_2/F_1	0.006	0.019	0.029	0.091	1.000
no. lines	464	463	365	413	31
avg. depth	0.2	0.23	0.11	0.12	0.10
cont. depth ^a	0.0012	0.0043	0.0031	0.0100	0.0833 ^b
SNR	833	232	323	100	12

^a avg. depth $\times F_2/(F_1 + F_2)$, where F_1 is the component in the far right column.

^b avg. depth $\times F_1/(F_1 + F_2)$, where F_2 is for the companion with $T_{\text{eff}}=3200$, $\log g=4.5$.

SNR >800 would be required to detect the individual spectral lines of the companion. With the SNR increasing with \sqrt{N} this would require the observational time for each target to be increased by a factor of $\sim 10\text{--}64$.

Our non-detection of binary companions with low flux ratios is consistent with other works. For example Nemravová et al. (2016) performed extensive spectral analysis of a quadruple-star system ξ Tauri using 227 spectra in 3 different wavelength bands with $R = 10\,000 - 48\,000$. Of the four stars in the system they were unable to detect the spectral component of the star which had a luminosity ratio below 1%.

7.3.3 χ^2 asymmetry

To try and understand **this** recovered companions further investigation into the χ^2 space was performed of the HD30501 synthetic simulation. The minimum χ^2 contours achieved for each companion temperature in the grid, regardless of rv_2 are shown in Figure 7.6. This is done for seven different injected companion temperatures, $T_{\text{eff}2}$, between 2500 and 4500 K. For the higher temperature companions, the χ^2 is parabolic in shape, recovering the correct temperature, as expected. At lower temperatures there is a strong asymmetry in the χ^2 with it flattening out on the lower temperature side. The 1-, 2-, 3- σ values (with two degrees of freedom) of 2, 6 and 11 above the minimum χ^2 are not shown in the bottom panel of Figure 7.6 which is a close-up around the minimum χ^2 as they are indistinguishable in the top panel

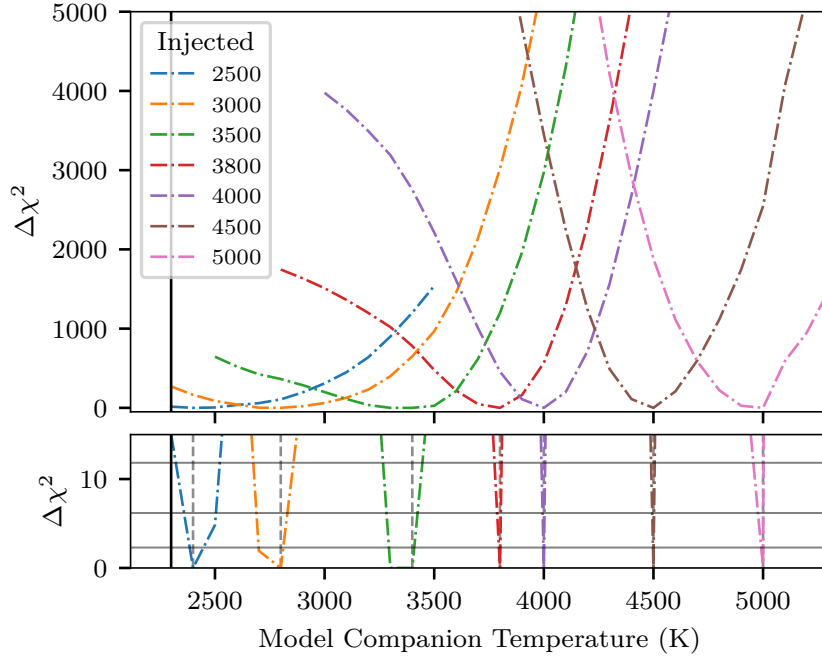


Figure 7.6: Top: Companion temperature versus χ^2 for simulations with different injected companion temperatures. The other fixed parameters for these fully synthetic simulations was $T_{\text{eff}1} = 5200$ K, $\log g_1 = 4.5$, $\log g_2 = 5.0$, and both $[\text{Fe}/\text{H}] = 0.0$. A fixed Gaussian noise corresponding to a SNR of 300 was used. Bottom: A close up view of χ^2 below 15. The three horizontal grey lines indicate the 1-, 2-, 3- σ with two degrees of freedom. The vertical dotted lines indicate the location of the minimum χ^2 recovered for each companion. The black solid vertical line in both panels shows the 2300 K cut-off of the PHOENIX-ACES models

due to the extreme χ^2 y-scale. The black vertical line indicates the 2300 K temperature limit of the PHOENIX-ACES models.

Figure 7.6 shows that the shape of the recovered χ^2 becomes asymmetric when dealing with companion temperatures below around 3800 K. A visual inspection of the spectra reveals the likely cause. In Figure 7.7 the spectra corresponding to the injected companions are shown between 2111–2165 nm. In the spectra, as the temperature decreases the strongest lines become less prominent, disappearing progressively among the other many small lines that appear at lower temperatures. At lower temperatures there are no strong companion lines to easily distinguish one temperature from another. In the flatter part of the χ^2 curves several low temperature companions are almost equally well fitted to the simulation/observation.

Figures 7.5 and 7.6 show slightly different recovered temperatures but both agree above 3800 K. A higher companion temperature is recovered between 2800 and 3800 K, where as in Figure 7.6 a lower temperature is recovered. This is probably due to a combination of the level of noise added, and the asymmetries of the χ^2 lines. Figure 7.5 uses the noise level measured from the observed spectrum while Figure 7.6 has a SNR of 300. This large asymmetry observed can also explain the jump observed in the synthetic recovery temperature around 2700 K in Figure 7.5.

The asymmetry also causes an asymmetry in the confidence level bounds which can be seen in the bottom panel of Figure 7.6. For instance the recovered value and 1- σ error bars on the 3000 K injected companion is 2800^{+20}_{-100} , with an asymmetric error bar skewed towards lower temperatures.

There is a slight bump observed at 5100 K in the χ^2 curves for the injected companions of 4500 and 5000 K. This is believed to be due to a discontinuity in the PHOENIX-ACES modelling. The “reference wavelength defining the mean optical depth grid” is changed at 5000 K (Husser et al., 2013, Section 2.3). More care needs to be taken if trying to detect a companion near this temperature.

7.3.4 Component RV separation

Another factor which could contribute to an unsuccessful detection is the RV separation between the host and companion, is rv_2 . Estimates for the observations are given in the last column of Table 6.3. If rv_2 is small compared to the line width, then all the same lines of both components will be blended. For example, (Kolbl et al., 2015) have difficulty separating blended spectra which have a component RV separation below 10 km s^{-1} . This is indeed the case for HD 4747, HD 211847, and HD 202206 with expected $|rv_2| < 2 \text{ km s}^{-1}$. This may have contributed to the lack of recovery with both components of the binary model trying to fit to the same features. This may even cause some correlation between the parameters of the two components. The RV separation of the two components changes with orbital phase. Having multiple spectra of the same target distributed in phase may allow the RV of the spectral components to be better recovered (e.g. Czekala et al., 2017; Sablowski et al., 2016; Piskorz et al., 2016).

7.3.5 Wavelength range

The wavelength choice for the spectra analysed here, observed with the intention to apply the spectral differential technique, was selected due to the location of the *K*-band telluric absorption window. This wavelength range, with a narrow wavelength range $\sim 50 \text{ nm}$ set by the CRIRES instrument. This wavelength range is not the best choice for the techniques applied here.

For instance Passegger et al. (2016) used four different spectral regions for the precise parameter determination of M-dwarfs using χ^2 methods. Specific lines in the different wavelength regions are

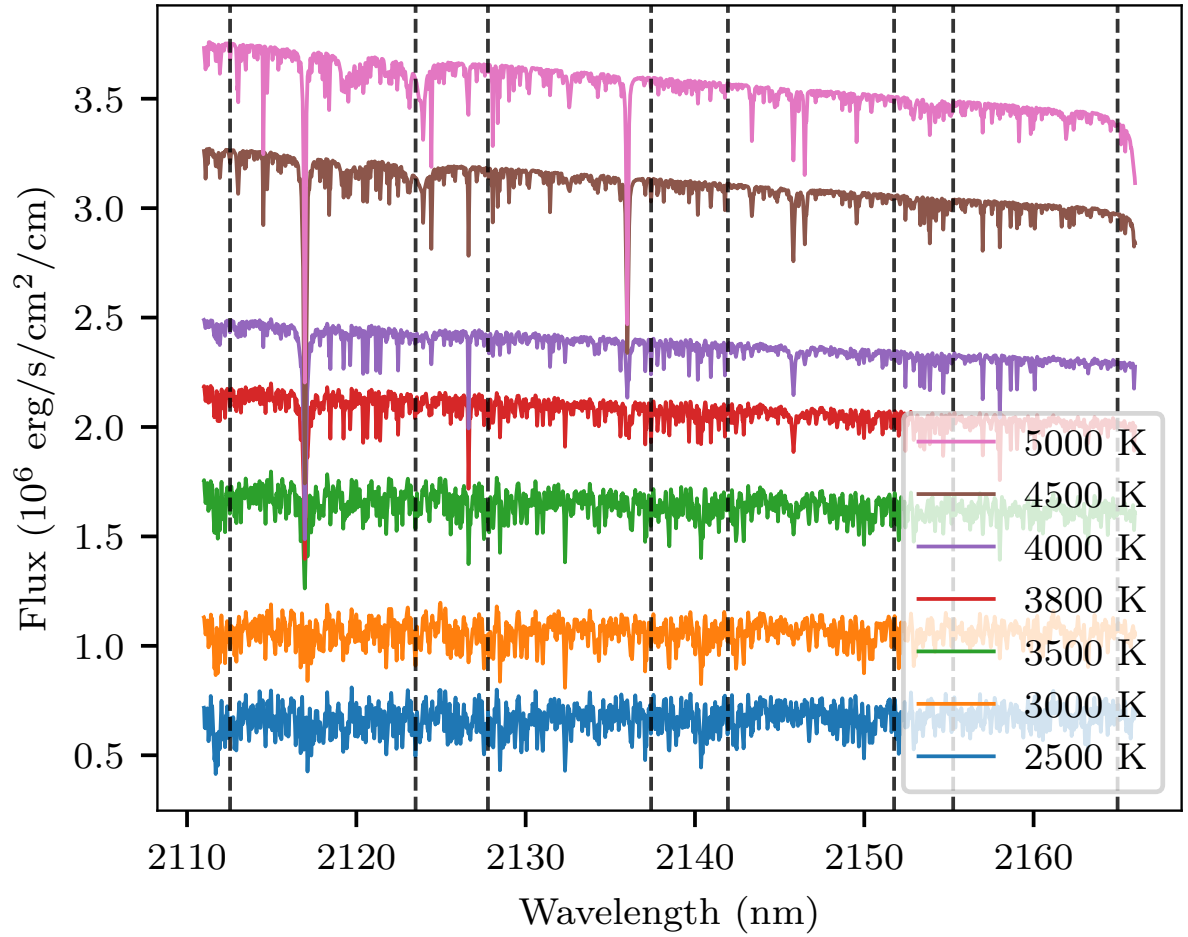


Figure 7.7: PHOENIX-ACES spectra for temperatures between 2500 and 5000 K, corresponding to the same lines in Figure 7.6. The flux units are the native units of the PHOENIX-ACES spectrum, ($\text{erg s}^{-1} \text{cm}^2 \text{cm}^{-1}$), and have not been scaled by the stellar radii. All spectra have a $\log g=5.0$ and $[\text{Fe}/\text{H}]=0.0$. The vertical dotted lines indicate the edges of the CRRES detectors.

affected differently by the model parameters: T_{eff} , $\log g$, and $[\text{Fe}/\text{H}]$; and are used to break degeneracies in the PHOENIX-ACES parameter space.

Changing the wavelength coverage to regions with lines sensitive to stellar parameters for both stars and BDs, as well as using a larger wavelength range that will be achieved by CRIRES+, may help to improve the recovery results of the companion recovery technique presented here.

Several works (e.g. Brogi et al., 2014; Brogi et al., 2016; Piskorz et al., 2016) have had successful molecule and companion detections in the wavelength range around 2300 nm due to strong CO lines. This wavelength region has already been shown to be promising for simulations of the differential technique in Kostogryz et al. (2013). This is clearly one wavelength region in particular to focus attention in the future.

7.3.6 The BT-Settl models

The PHOENIX-ACES models were not the only spectral libraries available with the other notable library considered for this work being the BT-Settl models (Allard et al., 2010; Allard, 2013; Baraffe et al., 2015) (see Section 4.3.2).

As the BT-Settl models are suitable to model the atmospheres of the brown dwarfs they would have been useful for the companion recovery technique developed here. However, as shown in Sections 7.2.2 and 7.2.3, a successful recovery of the $155 M_{\text{Jup}}$ ($T_{\text{eff}} \sim 3200 \text{ K}$) low mass star companion of HD 211847 was not possible. Limiting the temperature and derived a temperature upper limit for this method to around 3800 K. These are both well above the 2300 K cut-off of the PHOENIX-ACES models and for the onset of dust- and cloud-formation phenomena, at 2600 K.

As shown in Section 4.3.4 the PHOENIX-ACES and BT-Settl spectra are fairly similar. Figure 7.8 shows again the minimum χ^2 solution for detector #1 of the second HD 211847 observation, this time including the BT-Settl solution with the same parameters. Although the PHOENIX-ACES and BT-Settl models differ slightly they both have large spectral discrepancies to the observations. As such the BT-Settl models were not used in the χ^2 simulations and results as there did not seem to be any special advantage in using them. If promising results had been obtained with the PHOENIX-ACES, or a substantial difference between the synthetic spectral models more focus on the BT-Settl models would have occurred.

7.3.7 Impact of $\log g$

The surface gravity of a star, measured as $\log g$, is related to evolutionary state and the size of the star. Smaller $\log g$ values usually indicate bigger stars with larger radii. This parameter has a large impact on the radius and thus flux ratio of the binary models. In experimenting with the $\log g$ value of the PHOENIX-ACES models a decrease in $\log g$ from 5.0 to 4.5 increases the models effective radius by ~ 1.75 in the temperature range investigated here. This change in radius alone roughly triples the absolute flux of the synthetic spectrum (1.75^2), neglecting any changes to the shape of the actual spectrum. Therefore, there are large jumps in the model flux ratios, and the χ^2 solutions if the $\log g$ is allowed to vary. Like with higher companion temperatures, a lower $\log g$ value for the companion is favoured as the increased flux ratio reduces the spectral mismatch of the host component to the observations. This large impact of $\log g$ on the spectral library absolute flux is one reason for keeping the $\log g$ of each component fixed in the χ^2 results presented in Section 7.2.

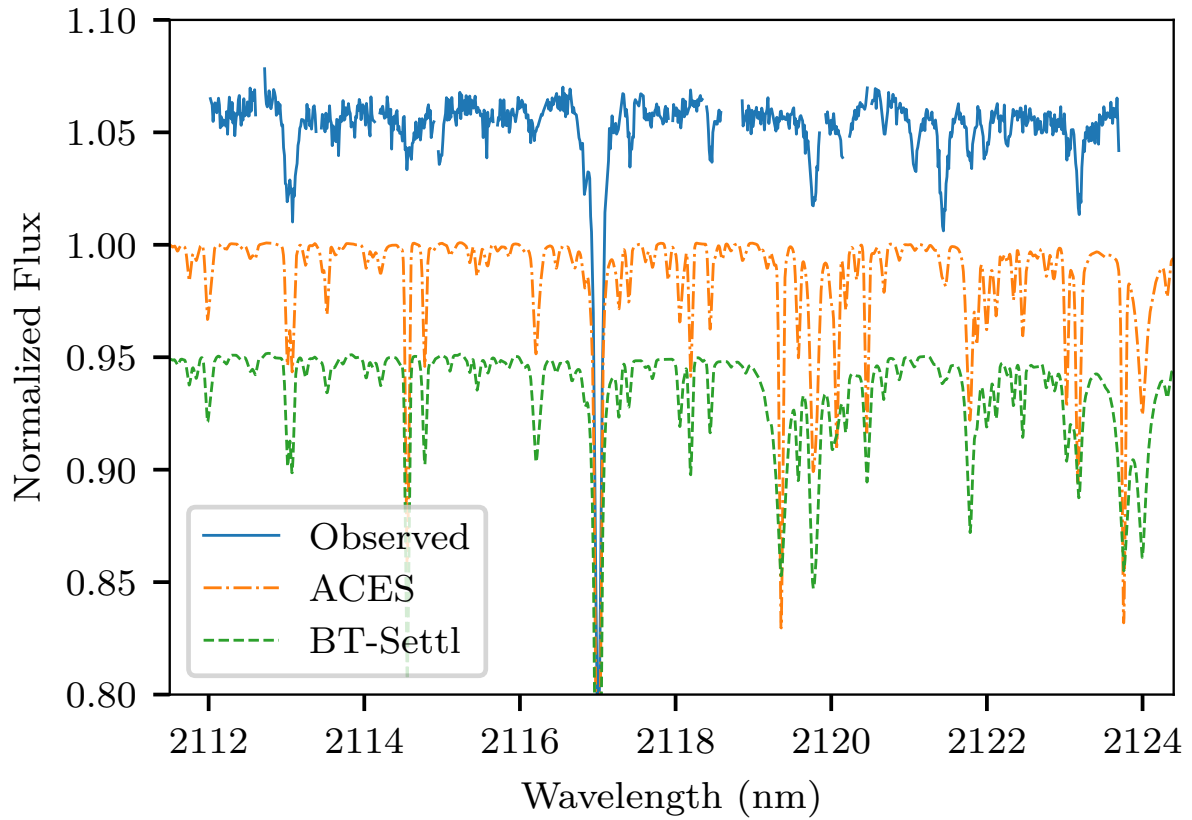


Figure 7.8: Detector #1 spectrum for HD 211847 (blue) alongside the PHOENIX-ACES (orange dash-dot) and BT-Settl (green dashed) synthetic spectra for the host star only, with parameters $T_{\text{eff}}=5700$ K, $\log g=4.5$ and $[\text{Fe}/\text{H}]=0.0$. Both synthetic models have been normalized and convolved to $R = 50\,000$. There is a 0.05 off-set between each spectrum

7.3.8 Interpolation

One procedure not incorporate into this χ^2 procedure is spectral interpolation between spectral grid points. It is common to interpolate between the synthetic spectral grids to fit and derive parameters in between the grid points such as performed in Nemravová et al. (2016) and Passegger et al. (2016). At a more advanced stage, instead of interpolation, Czekala et al., 2015 use a spectral emulator and use Principal Component Analysis to create eigenspectra for the synthetic library and Gaussian processes to derive a probability distribution function of possible interpolation spectra to account for uncertainties in the interpolation required for high signal-to-noise spectra.

Interpolation could be something to be added to this work in the future to refine the recovered parameters, and to help the transition between the grid $\log g$ values. Codes are readily available to perform spectral interpolation which could be utilized for this, two of them are *pyterpol*⁷ Nemravová et al. (2016) and *Starfish*⁸ Czekala et al., 2015.

7.3.9 Contrast to other works

In this work the techniques attempted were unsuccessful in detecting the companions. Here some relevant comparisons are made to recent positive detections in the literature.

Passegger et al. (2016) apply χ^2 fitting of M-dwarf spectra in the nIR to PHOENIX-ACES models, incorporating inter-grid interpolation to determine M-dwarf parameters. Reaching a level inherent uncertainties on the parameters of $\sigma_{T_{\text{eff}}} = 35 \text{ K}$, $\sigma_{\log g} = 0.14$, and $\sigma_{[\text{Fe}/\text{H}]} = 0.11$, on four stars. Passegger et al. (2018) further extend this method to the 300 stars of the CARMENES library with optical and nIR spectra, achieving uncertainties of $\sigma_{T_{\text{eff}}} = 51 \text{ K}$, $\sigma_{\log g} = 0.07$ and $\sigma_{[\text{Fe}/\text{H}]} = 0.16$. The temperatures recovered are in line with the literature values while their metallicity determination has a larger spread when compared to the literature. These uncertainties are much smaller than the library grid spacing due to the fine-grid search achieved by interpolation. Rajpurohit et al. (2018) perform similar parameter determination, using the recent BT-Settl models instead, exploring more lower temperature M-dwarfs than Passegger et al. (2018), at which point dust clouds begin to form. The results of Rajpurohit et al. (2018) are in agreement with (Gaidos et al., 2014) but they find a disagreement to the Passegger et al. (2018) parameters, particularly T_{eff} , with up to a 200–300 K difference between the PHOENIX-ACES and BT-Settl results. Differences are also observed between the $\log g$ and $[\text{Fe}/\text{H}]$ recovered by the two works. Both these works use a much larger wavelength range ($\sim 500\text{--}1700 \text{ nm}$) than utilized here.

In trying to detect secondary stellar spectra in optical spectra at $R = 60\,000$, (Kolbl et al., 2015) are able to detect secondary spectra down to a 1% flux ratio, by matching to a library of real spectra. The work performed here aimed at flux ratios starting around below this limit, even after taking advantage of the increased flux ratio in the nIR.

One promising technique with a success in detecting faint companion emission spectra is presented by Lockwood et al. (2014). Applying the TODCOR correlation to several spectra at different epochs and combining the observations while accounting for the orbits using a maximum likely-hood framework. They confirm the water emission signature in τ Boötis and find a 1σ upper limit high resolution ($R = 24\,000$) spectroscopic flux ratio of 10^{-4} at $3.3 \mu\text{m}$.

(Piskorz et al., 2016) used this same technique to achieve a detection of a non-transiting hot gas giant HD 88133b, with a flux ratio near 10^{-5} . This is achieved with spectra from nine epochs, six in the L -band

⁷ <https://github.com/chrysante87/pyterpol>

⁸ <https://github.com/iancze/Starfish>

and three epochs in the K -band with the Keck NIRPSEC instrument ($R=25\,000\text{--}30\,000$). Each epoch has a combined exposure time of 60–180 minutes reaching a SNR between 1600–3000 allowing for the planetary emission spectra to be recovered around a flux ratio of 10^{-5} .

These successful works clearly reveal the difficulty faced with the spectra analysed in this current work. Particularly, the SNR in (Piskorz et al., 2016) is an order of magnitude higher and the wavelength coverage is significantly larger, due to the cross-dispersion of NIRPSEC. Also the multi-epoch approach allows for the RV of the two components to be monitored and some orbital parameters determined. The narrow wavelength coverage CRIRES spectra analysed here, at SNR=100–300 are insufficient. The poorly separated epochs, were also a problem as addressed in Section 6.4.

7.4 Summary

After attempting two different methods to detect the companion BDs these observations were abandoned...

Is another summary needed here? transition to next chapter

Precision table
needs fixed up

Bibliography

- Adibekyan, V. Z., S. G. Sousa, N. C. Santos, E. D. Mena, et al. (2012). “Chemical Abundances of 1111 FGK Stars from the HARPS GTO Planet Search Program - Galactic Stellar Populations and Planets”. In: *Astronomy and Astrophysics* 545, A32.
- Allard, F. (2013). “The BT-Settl Model Atmospheres for Stars, Brown Dwarfs and Planets”. In: *Proceedings of the International Astronomical Union* 8.S299. 00007, pp. 271–272.
- Allard, F., D. Homeier, and B. Freytag (2010). “Model Atmospheres From Very Low Mass Stars to Brown Dwarfs”. In: 00066. arXiv: 1011.5405 [astro-ph].
- Astudillo-Defru, N., X. Bonfils, X. Delfosse, D. Ségransan, et al. (2015). “The HARPS Search for Southern Extra-Solar Planets. XXXVI. Planetary Systems and Stellar Activity of the M Dwarfs GJ 3293, GJ 3341, and GJ 3543”. In: *Astronomy and Astrophysics* 575, A119.
- Bagnuolo Jr., W. G. and D. R. Gies (1991). “Tomographic Separation of Composite Spectra - The Components of the O-Star Spectroscopic Binary AO Cassiopeiae”. In: *The Astrophysical Journal* 376, pp. 266–271.
- Baraffe, I., G. Chabrier, T. Barman, F. Allard, and P. H. Hauschildt (2003). “Evolutionary Models for Cool Brown Dwarfs and Extrasolar Giant Planets. The Case of HD 20945”. In: *Astronomy and Astrophysics* 402.2. 00000, pp. 701–712. arXiv: astro-ph/0302293.
- Baraffe, I., D. Homeier, F. Allard, and G. Chabrier (2015). “New Evolutionary Models for Pre-Main Sequence and Main Sequence Low-Mass Stars down to the Hydrogen-Burning Limit”. In: *Astronomy and Astrophysics* 577. 00280, A42. arXiv: 1503.04107.
- Barnes, J. R., T. S. Barman, H. R. A. Jones, C. J. Leigh, A. C. Cameron, R. J. Barber, and D. J. Pinfield (2008). “HD 179949b: A Close Orbiting Extrasolar Giant Planet with a Stratosphere?” In: *Monthly Notices of the Royal Astronomical Society* 390.3, pp. 1258–1266.
- Benedict, G. F. and T. E. Harrison (2017). “HD 202206: A Circumbinary Brown Dwarf System”. In: *The Astronomical Journal* 153, p. 258.
- Bevington, P. R. and D. K. Robinson (2003). *Data Reduction and Error Analysis for the Physical Sciences*. p.g. 208-212. McGraw-Hill. 320 pp.
- Bonfanti, A., S. Ortolani, and V. Nascimbeni (2016). “Age Consistency between Exoplanet Hosts and Field Stars”. In: *Astronomy and Astrophysics* 585, A5.
- Brogi, M., R. J. de Kok, S. Albrecht, I. A. G. Snellen, J. L. Birkby, and H. Schwarz (2016). “Rotation and Winds of Exoplanet HD 189733 b Measured with High-Dispersion Transmission Spectroscopy”. In: *The Astrophysical Journal* 817.2. 00000, p. 106. arXiv: 1512.05175.

- Brogi, M., R. J. de Kok, J. L. Birkby, H. Schwarz, and I. A. G. Snellen (2014). “Carbon Monoxide and Water Vapor in the Atmosphere of the Non-Transiting Exoplanet HD 179949 B”. In: *Astronomy and Astrophysics* 565. 00000, A124.
- Collaboration, G., A. G. A. Brown, A. Vallenari, T. Prusti, et al. (2018). “Gaia Data Release 2. Summary of the Contents and Survey Properties”. In: *ArXiv e-prints*, arXiv:1804.09365.
- Correia, A. C. M., S. Udry, M. Mayor, J. Laskar, et al. (2005). “The CORALIE Survey for Southern Extra-Solar Planets. XIII. A Pair of Planets around HD 202206 or a Circumbinary Planet?” In: *aap* 440. 00000, pp. 751–758.
- Crepp, J. R., E. J. Gonzales, E. B. Bechter, B. T. Montet, et al. (2016). “The TRENDS High-Contrast Imaging Survey. VI. Discovery of a Mass, Age, and Metallicity Benchmark Brown Dwarf”. In: *The Astrophysical Journal* 831. 00004.
- Czekala, I., S. M. Andrews, K. S. Mandel, D. W. Hogg, and G. M. Green (2015). “Constructing A Flexible Likelihood Function For Spectroscopic Inference”. In: *The Astrophysical Journal* 812.2. 00022, p. 128. arXiv: 1412.5177.
- Czekala, I., K. S. Mandel, S. M. Andrews, J. A. Dittmann, S. K. Ghosh, B. T. Montet, and E. R. Newton (2017). “Disentangling Time-Series Spectra with Gaussian Processes: Applications to Radial Velocity Analysis”. In: *The Astrophysical Journal* 840.1. 00002, p. 49.
- Czesla, S., T. Molle, and J. H. M. M. Schmitt (2018). “A Posteriori Noise Estimation in Variable Data Sets. With Applications to Spectra and Light Curves”. In: *Astronomy and Astrophysics* 609, A39.
- Deeg, H. (1998). “Photometric Detection of Extrasolar Planets by the Transit-Method”. In: *Brown Dwarfs and Extrasolar Planets*. Brown Dwarfs and Extrasolar Planets. Vol. 134. ASP Conference Series #134, p. 216.
- ESO (2017). *ESO Call for Proposals - P101*.
- Ferluga, S., L. Floreano, U. Bravar, and C. Bédalo (1997). “Separating the Spectra of Binary Stars-I. A Simple Method: Secondary Reconstruction”. In: *Astronomy and Astrophysics Supplement Series* 121.1. 00012, pp. 201–209.
- Figueira, P., V. Z. Adibekyan, M. Oshagh, J. J. Neal, et al. (2016). “Radial Velocity Information Content of M Dwarf Spectra in the Near-Infrared”. In: *Astronomy and Astrophysics* 586. 00002, A101.
- Gaidos, E. and A. W. Mann (2014). “M Dwarf Metallicities and Giant Planet Occurrence: Ironing Out Uncertainties and Systematics”. In: *The Astrophysical Journal* 791.1, p. 54.
- González, J. F. and H. Levato (2006). “Separation of Composite Spectra: The Spectroscopic Detection of an Eclipsing Binary Star”. In: *Astronomy and Astrophysics* 448, pp. 283–292.
- Hadrava, P. (1995). “Orbital Elements of Multiple Spectroscopic Stars.” In: *Astronomy and Astrophysics Supplement Series* 114, p. 393.
- (2009). “Disentangling of Spectra - Theory and Practice”. In: 00013. arXiv: 0909.0172 [astro-ph].
- Husser, T.-O., S. W.-. von Berg, S. Dreizler, D. Homeier, A. Reiners, T. Barman, and P. H. Hauschildt (2013). “A New Extensive Library of PHOENIX Stellar Atmospheres and Synthetic Spectra”. In: *Astronomy and Astrophysics* 553. 00243, A6. arXiv: 1303.5632.
- Kaeufl, H.-U., P. Ballester, P. Biereichel, B. Delabre, et al. (2004). “CRIRES: A High-Resolution Infrared Spectrograph for ESO’s VLT”. In: *Ground-based Instrumentation for Astronomy* 5492. 00000, p. 1218.
- Kolbl, R., G. W. Marcy, H. Isaacson, and A. W. Howard (2015). “Detection of Stars Within ~ 0.8 in of Kepler Objects of Interest”. In: *The Astronomical Journal* 149, p. 18.

- Kostogryz, N., M. Kürster, T. Yakobchuk, Y. Lyubchik, and M. Kuznetsov (2013). “A Spectral Differential Approach to Characterizing Low-Mass Companions to Late-Type Stars”. In: *Astronomische Nachrichten* 334.7. 00000, pp. 648–660.
- Ku, H. H. (1966). *Notes on the Use of Propagation of Error Formulas*. National Bureau of Standards.
- Lockwood, A. C., J. A. Johnson, C. F. Bender, J. S. Carr, T. Barman, A. J. W. Richert, and G. A. Blake (2014). “Near-IR Direct Detection of Water Vapor in Tau Boötis B”. In: *The Astrophysical Journal Letters* 783.2. 00038, p. L29.
- López-Morales, M., R. D. Haywood, J. L. Coughlin, L. Zeng, et al. (2016). “Kepler-21b: A Rocky Planet Around a $V = 8.25$ Magnitude Star”. In: *The Astronomical Journal* 152, p. 204.
- Martins, J. H. C., N. C. Santos, P. Figueira, J. P. Faria, et al. (2015). “Evidence for a Spectroscopic Direct Detection of Reflected Light from 51 Pegasi B”. In: *Astronomy and Astrophysics* 576, A134.
- Mazeh, T., E. L. Martin, D. Goldberg, and H. A. Smith (1997). “Detecting Faint Secondaries of Spectroscopic Binaries: HD 101177B and 149414A”. In: *Monthly Notices of the Royal Astronomical Society* 284.2. 00014, pp. 341–347.
- Mazeh, T. and S. Zucker (1994). “Todcor: A Two-Dimensional CORrelation Technique to Analyze Stellar Spectra in Search of Faint Companions”. In: *Astrophysics and Space Science* 212.1, pp. 349–356.
- Melo, C., N. C. Santos, W. Gieren, G. Pietrzynski, et al. (2007). “A New Neptune-Mass Planet Orbiting HD 219828”. In: *Astronomy and Astrophysics* 467, pp. 721–727.
- Ment, K., J. A. Dittmann, N. Astudillo-Defru, D. Charbonneau, et al. (2018). “A Second Planet with an Earth-like Composition Orbiting the Nearby M Dwarf LHS 1140”. In: *ArXiv e-prints* 1808, arXiv:1808.00485.
- Moutou, C., A. Vigan, D. Mesa, S. Desidera, P. Thébault, A. Zurlo, and G. Salter (2017). “Eccentricity in Planetary Systems and the Role of Binarity - Sample Definition, Initial Results, and the System of HD 211847”. In: *Astronomy and Astrophysics* 602. 00001, A87.
- Murray, C. D. and A. C. M. Correia (2010). “Keplerian Orbits and Dynamics of Exoplanets”. In: *Exoplanets*. Ed. by S. Seager. 00000. University of Arizona Press, pp. 15–23.
- Nemravová, J. A., P. Harmanec, M. Brož, D. Vokrouhlický, et al. (2016). “ ξ Tauri: A Unique Laboratory to Study the Dynamic Interaction in a Compact Hierarchical Quadruple System”. In: *Astronomy and Astrophysics* 594, A55.
- Passegger, V. M., A. Reiners, S. V. Jeffers, S. Wende-von Berg, et al. (2018). “The CARMENES Search for Exoplanets around M Dwarfs. Photospheric Parameters of Target Stars from High-Resolution Spectroscopy”. In: *Astronomy and Astrophysics* 615, A6.
- Passegger, V. M., S. W.-v. Berg, and A. Reiners (2016). “Fundamental M-Dwarf Parameters from High-Resolution Spectra Using PHOENIX ACES Models: I. Parameter Accuracy and Benchmark Stars”. In: *Astronomy and Astrophysics* 587. 00006, A19. arXiv: 1601.01877.
- Pepe, F., A. C. Cameron, D. W. Latham, E. Molinari, et al. (2013). “An Earth-Sized Planet with an Earth-like Density”. In: *Nature* 503, pp. 377–380.
- Pilyavsky, G., S. Mahadevan, S. R. Kane, A. W. Howard, et al. (2011). “A Search for the Transit of HD 168443b: Improved Orbital Parameters and Photometry”. In: *apj* 743, 162. 00014, p. 162.
- Piskorz, D., B. Benneke, N. R. Crockett, A. C. Lockwood, et al. (2016). “Evidence for the Direct Detection of the Thermal Spectrum of the Non-Transiting Hot Gas Giant HD 88133 B”. In: *The Astrophysical Journal* 832.2, p. 131.

- Queloz, D., F. Bouchy, C. Moutou, A. Hatzes, et al. (2009). “The CoRoT-7 Planetary System: Two Orbiting Super-Earths”. In: *Astronomy & Astrophysics* 506.1, pp. 303–319.
- Rajpurohit, A. S., F. Allard, S. Rajpurohit, R. Sharma, G. D. C. Teixeira, O. Mousis, and R. Kamlesh (2018). “Exploring the Stellar Properties of M Dwarfs with High-Resolution Spectroscopy from the Optical to the near-Infrared”. In: *Astronomy and Astrophysics* 620, A180.
- Rajpurohit, A. S., C. Reyl  , F. Allard, D. Homeier, et al. (2016). “Spectral Energy Distribution of M-Subdwarfs: A Study of Their Atmospheric Properties”. In: *Astronomy and Astrophysics* 596, A33.
- Rodler, F., M. Lopez-Morales, and I. Ribas (2012). “Weighing the Non-Transiting Hot Jupiter τ Boo B”. In: *The Astrophysical Journal Letters* 753.1. 00077, p. L25.
- Sablowski, D. P. and M. Weber (2016). “Spectral Disentangling with Spectangular”. In: *Astronomy and Astrophysics*. 00000.
- Sahlmann, J., D. Segransan, D. Queloz, S. Udry, et al. (2011). “Search for Brown-Dwarf Companions of Stars”. In: *Astronomy and Astrophysics* 525. 00115, A95. arXiv: 1009.5991.
- Sanchis-Ojeda, R., J. N. Winn, and D. C. Fabrycky (2013). “Starspots and Spin-Orbit Alignment for Kepler Cool Host Stars”. In: *Astronomische Nachrichten* 334.1-2, pp. 180–183. arXiv: 1211.2002.
- Santos, N. C., G. Israelian, and M. Mayor (2004). “Spectroscopic [Fe/H] for 98 Extra-Solar Planet-Host Stars. Exploring the Probability of Planet Formation”. In: *Astronomy and Astrophysics* 415, pp. 1153–1166.
- Santos, N. C., G. Israelian, M. Mayor, J. P. Bento, P. C. Almeida, S. G. Sousa, and A. Ecuivillon (2005). “Spectroscopic Metallicities for Planet-Host Stars: Extending the Samples”. In: *aap* 437. 00000, pp. 1127–1133.
- Santos, N. C., A. Santerne, J. P. Faria, J. Rey, et al. (2016). “An Extreme Planetary System around HD 219828. One Long-Period Super Jupiter to a Hot-Neptune Host Star”. In: *Astronomy and Astrophysics* 592, A13.
- Schwarz, G. (1978). “Estimating the Dimension of a Model”. In: *The Annals of Statistics* 6.2, pp. 461–464.
- Simon, K. P. and E. Sturm (1994). “Disentangling of Composite Spectra”. In: *Astronomy and Astrophysics* 281. 00000, pp. 286–291.
- Sorahana, S., I. Yamamura, and H. Murakami (2013). “On the Radii of Brown Dwarfs Measured with AKARI Near-Infrared Spectroscopy”. In: *The Astrophysical Journal* 767.1, p. 77. arXiv: 1304.1259.
- Sousa, S. G., N. C. Santos, M. Mayor, S. Udry, et al. (2008). “Spectroscopic Parameters for 451 Stars in the HARPS GTO Planet Search Program. Stellar [Fe/H] and the Frequency of Exo-Neptunes”. In: *aap* 487. 00390, pp. 373–381.
- Tsantaki, M., S. G. Sousa, V. Z. Adibekyan, N. C. Santos, A. Mortier, and G. Israelian (2013). “Deriving Precise Parameters for Cool Solar-Type Stars. Optimizing the Iron Line List”. In: *aap* 555, A150. 00077, A150.
- Udry, S., M. Mayor, D. Naef, F. Pepe, D. Queloz, N. C. Santos, and M. Burnet (2002). “The CORALIE Survey for Southern Extra-Solar Planets: VIII. The Very Low-Mass Companions of HD 141937, HD 162020, HD 168443 and HD 202206: Brown Dwarfs or “Superplanets”?” In: *Astronomy and Astrophysics* 390.1. 00158, pp. 267–279.
- Wenger, M., F. Ochsenbein, D. Egret, P. Dubois, et al. (2000). “The SIMBAD Astronomical Database. The CDS Reference Database for Astronomical Objects”. In: *Astronomy and Astrophysics Supplement Series* 143, pp. 9–22.

- Zechmeister, M., A. Reiners, P. J. Amado, M. Azzaro, et al. (2018). “Spectrum Radial Velocity Analyser (SERVAL). High-Precision Radial Velocities and Two Alternative Spectral Indicators”. In: *Astronomy and Astrophysics* 609, A12.
- Zucker, S. and T. Mazeh (1994). “Study of Spectroscopic Binaries with TODCOR. 1: A New Two-Dimensional Correlation Algorithm to Derive the Radial Velocities of the Two Components”. In: *The Astrophysical Journal* 420. 00376, pp. 806–810.